Applied Ocean Research 64 (2017) 135–154

Contents lists available at ScienceDirect

Applied Ocean Research

journal homepage: www.elsevier.com/locate/apor

Experimental and numerical hydrodynamic analysis of a stepped planing hull

Agostino De Marco, Simone Mancini, Salvatore Miranda, Raffaele Scognamiglio, Luigi Vitiello*

Department of Industrial Engineering, University of Napoli Federico II, Italy

ARTICLE INFO

Article history:
Received 16 July 2016
Received in revised form 2 January 2017
Accepted 13 February 2017

Keywords:
Ship hydrodynamics
Stepped hull
Towing tank test
CFD simulation
Overset/chimera grid
Morphing grid

ABSTRACT

This work addresses the experimental and numerical study of a stepped planing hull and the related fluid dynamics phenomena typically occurring in the stepped hull in the unwetted aft body area behind the step. In the last few years, the interest in high-speed planing crafts, with low weight-to-power ratios, has been increasing significantly, and, in such context, naval architects have been orienting toward the stepped hull solution. Stepped planing hulls ensure good dynamic stability and seakeeping qualities at high speeds. This is mainly due to the reduction of the wetted area, which is caused by the flow separation occurring at the step. This paper presents the experimental results of towing tank tests in calm water on a single-step hull model, which is the first model of a new systematic series. The same flow conditions are analyzed via Reynolds Averaged Navier-Stokes (RANS) and Large Eddy Simulations (LES), with different moving mesh techniques (overset/chimera and morphing grid), performed at different model speeds. The numerical results are in accordance with experimental data, and overset/chimera grid is found to be the best approach between the analyzed ones. The flow patterns obtained numerically through LES on a refined grid appear similar to the ones observed in towing tank investigations through photographic acquisitions. These flow patterns are dominated by a rather complex 3D arrangement of vortices originating from air spillage at both sides of the step. The understanding of these phenomena is important for the effectiveness of stepped hull designs.

1. Introduction

In the last few years, the development of lightweight engines and propulsion systems, along with the development of lighter boats built by shipyards with new technology and materials, has forced designers to pay increasing attention to hull design. Outboard engines in particular are characterized nowadays by a very low weight to power ratio and high reliability. These features make them suitable for several installation types, including military, commercial, pleasure, and racing. The new composite materials allow a boat weight reduction of 30% with respect to a traditional hand-made layup. In this scenario in recent years, the high-speed planing craft for military, commercial, and pleasure use, with a very low weight to power ratio has spread even further.

The reduction of weight to power ratio involves an increase of maximum speed; as a consequence, naval architects are oriented even more in stepped hull design to reduce the resistance at high speed and ensuring good dynamic stability and seakeeping. The step is a sharp discontinuity located in the bottom surface of the hull; it is transversal and usually V-shaped, with the vertex facing aftward, on the outboard sides of the hull the step terminates with large apertures (also named 'inlets') for incoming air.

As pointed out by [1], the stepped hull is characterized by a low hydrodynamic drag-to-lift ratio at high speeds and by a wetted area reduction due to a flow separation, which occurs at step location and then reattaches at the aft body [2]. Moreover, stepped planing hulls have a small variability of trim angle and improve control of the longitudinal attitude because they are sailed always on a $n+1$ wetted triangle, where n represents the number of steps. In fact, for a single stepped hull, an additional aft-lift is created, due to the presence of the reattachment line (stagnation line) in the aft-body. This force keeps the running trim of the vessel almost constant with Froude number (at high speed). This feature is beneficial because avoids the porpoising instability, which occurs instead to stepless planing hulls.

* Corresponding author.
E-mail address: luigi.vitiello@unina.it (L. Vitiello).

http://dx.doi.org/10.1016/j.apor.2017.02.004
0141-1187/

Nomenclature

B	Breadth (m)
B_r	Bias systematic uncertainty
c_j	Basis constant
C_k	Correction factor
D	Vertex displacement
E	Comparison error
D	Experimental data
Fr_∇	Volumetric froude number
F_s	Factor of safety
Fr	Froude number
K	Constant value
L	Water line length (m)
L_{OA}	Length overall (m)
N	Number of control vertices
S_n	Numerical simulation result
p_k	Observed order of accuracy
P_r	Precision uncertainty
r_{ij}	Magnitude of distance between two vertices
r_k	Refinement ratio
R_k	Convergence ratio
R_{TM}	Total model resistance (N)
S	Wetted surface (m^2)
$SDev_j$	Standard deviation of j^{th} run
U	Uncertainty
U_r	Total uncertainty
U_k	k-input parameter uncertainty
U_I	Iterative uncertainty
U_G	Grid uncertainty
U_{TS}	Time step uncertainty
U_{SN}	Numerical simulation uncertainty
U_V	Validation uncertainty
U_D	Experimental data uncertainty
V	Hull speed (m/s)
Z	Sinkage (m)
∇	Displacement volume (m^3)

Greek symbols

A	Constant value
Δ	Displacement weight (N)
E	Solution change
P	Density (kg/m^3)
Λ	Expansion coefficient
Δt	Time step (s)
T	Dynamic trim angle (deg)

Acronyms

AIAA	American Institute of Aeronautics and Astronautics
AMG	Algebraic multi grid
ASME	American Society of Mechanical Engineer
CF	Correction Factor
CFD	Computational fluid dynamics
CFL	Courant Friedrichs Lewy number
CNC	Computer numerical control
DAQ	Data acquisition device
DFBI	Dynamic fluid body interaction
DOF	Degree of freedom
DT	Down thrust
EFD	Experimental fluid dynamics
FRP	Fiber reinforced plastic
GCI	Grid convergence index
HRIC	High resolution interface capturing scheme
ITTC	International Towing Tank Conference
LCB	Longitudinal centre of buoyancy
LCG	Longitudinal centre of gravity
LES	Large eddy simulation
NV	Numerical ventilation
PVC	Polyvinyl chloride
RANS	Reynolds average navier-Stokes
RBF	Radial basic function
RBM	Rigid body motion
RE	Richardson extrapolation
RIB	Rigid inflatable boat
RSS	Root sum square
SIMPLE	Semi implicit method pressure linked equations
UA	Uncertainty analysis
VOF	Volume of fluid
V&V	Verification and validation

Another way to obtain a hydrodynamic resistance reduction is the application of the artificial bottom cavities with side skegs. The state of the art of the air lubrication technologies together with research activities in Russia until 2010 can be found in Sverchkov [3].

Nowadays there are three options for the hydrodynamic analysis of stepped hulls: experimental testing, empirical estimation methods, and numerical simulations.

Experimental Fluid Dynamics (EFD) tests, that is towing tank tests, are very expensive and time consuming. Moreover, the only stepped hull systematic series experimental results available are those performed at the University of Southampton [4].

Two empirical hydrodynamic prediction methods are those published in [1] and [5]. The first method experimentally studied the longitudinal surface wake profiles aft of prismatic hulls; the second method combines the equations of [1] with the equations of Savitsky's method for conventional planing hulls for power prediction of a stepped hull.

Numerical methods, such as those based on Computational Fluid Dynamics (CFD) simulations, can be used nowadays to calculate the hydrodynamic performance of a stepped hull with good accuracy. In the last few years, several studies investigated this research field. Garland and Maki [6] conducted a numerical study on a 2D stepped planing surface. Their results showed that the lift-to-frictional-drag ratio varies very little with respect to the step location. Makasyeyev [7] developed a solution method for the 2D mathematical problem of planing of the stepped air cavity hulls. Matveev [8] applied hydrodynamic discrete sources for 2D modeling of stepped planing surfaces, calculating the water surface deformations, wetted hull lengths, and pressure distribution at given hull attitude and Froude number (Fr). Matveev, in another study [9], presented the steady hydrodynamic modeling of semi-planing hulls with pressurized and open air cavities. This method is based on a linearized potential-flow theory for surface flows. Brizzolara and Federici [10] developed an integrated semi-theoretical/numerical (CFD) method for the design of V-shaped stepped planing hulls that presented a considerable resistance reductions with respect to conventional hull forms. Lotfi [11] used an unsteady RANS solver (ANSYS-CFX) based on a Volume of Fluid (VoF) approach for examining the characteristics and performance of a planing hull having one transverse step. Similar research was conducted by Bakhtiari [12]. Moreover, an extended overview of the state of art of the simulations in the air layer drag reduction is reported in Stern et al. [13].

It is clear, nowadays, that CFD is becoming a fundamental support for hydrodynamic investigations in order to perform detailed analysis and to reduce the number of more expensive towing tank

tests. EFD however, are always necessary alongside validation of numerical results.

In this work, an integrated approach between EFD and CFD tests has been applied with the aim to investigate the quite complex hydrodynamic field generated by the stepped hull. All experimental and numerical tests were performed for a stepped hull in calm water. Several simulations were carried out with different meshing techniques in order to achieve good numerical convergence and to capture the vortical structures observed in towing tank tests.

The physics of the hydrodynamic field generated by the stepped hull are quite complex, more than planing craft. For this reason, particular attention has been paid in the unsteady RANS simulations of the resistance tests. Hence, more than one mesh approach has been used for the body motion simulation, such as the overset/chimera grid and morphing mesh technique [14]. In fact, planing/stepped hull performance is very sensitive to hull position (sinkage and trim) [15] as opposed to the displacement hull. For this reason, accurate simulations of the hull motion are necessary. Therefore, non-conventional approaches (*i.e.*: overset mesh and morphing grid) for the simulation of the hull motion are required, as indicated in [16].

Overset/chimera meshing allows bodies to move freely throughout the computational domain without being artificially constrained by the mesh. Two different mesh regions were used, *i.e.*, background mesh and body fitted mesh around the geometry of interest (overlapping meshes). The morphing mesh technique allows for complicated and arbitrary relative motion by morphing the nodes of the mesh. Typically, the mesh morphing can be used to model scenarios where components deform and change shape, (see Refs. [17] and [18] as examples of application in the marine field). However, this technique can also be employed for the Rigid Body Motion (RBM) case.

Furthermore, there is a lack of a satisfactory interpretation of the complicated flow phenomena in the separated region behind the step. This paper presents a detailed study of the vortex structures in the unwetted aft body area and their development into the downstream water flow by means of photographic acquisitions and Large Eddy Simulations (LES) on a refined grid.

The remaining part of this work is organized as follows: the experimental tests are presented in Section 2. The numerical model is presented and discussed in Section 3. In the same section, numerical simulations carried out by using both the overset/chimera grid and the morphing mesh approaches are also presented, including the results of a verification and validation study. The numerical results are compared with the experimental ones and discussed in Section 4. In Appendix A, Appendix B, Appendix C are reported, respectively, the laboratory instrumentation and measurement techniques, experimental, and numerical uncertainty analysis.

2. Experimental tests

2.1. Description of the model

The model used in this study represents an example of a modern high-speed hull for Rigid Inflatable Boats (RIB). This hull can be a representative hull for typical pleasure or military high-speed craft. This model is the hull number C03, one of the eight models of a systematic series now unpublished. The body plan of the C03 hull is reported in Fig. 1.

The parent hull for this research is a RIB built by MV Marine S.r.l., type Mito 31 powered with two outboard engines.

The model is a hard chine hull with one transverse step, located in the same longitudinal position of center of gravity with a forward V shape (Fig. 1). This shape of the step is different to the transverse bottom step and the arrow-like shape as reported in Sverchkov [3]. The hull considered in this study is a traditional stepped hull, without artificial bottom cavity, without artificially inflated air in the cavity, without skegs put on side of the cavity near the chine. The model has the same main dimensions (keel line, chine line, deadrise angle, displacement, LCG, step shape, step angle) of RIB Mito 31, with 1:10 scale.

Table 1
Model details.

Description	
Length over all: L_{OA} [m]	0.935
Breadth max: B_{MAX} [m]	0.335
Deadrise angle at transom [°] [°]	23
Step height [mm]	6
Displacement [N]	30.705
LCG [%*L*]	33
Model scale	1:10

Details of the hull model are reported in Table 1.

The model for towing tank tests was designed in 3D CAD and built with composite materials. The model has a transparent bottom built only with isophtalic resin to provide a full view of the water flow under the hull. The side of the model was built in Fiber Reinforced Plastic (FRP), and the model surface was built with high-gloss neopentilic gelcoat transparent.

The model was manufactured in hand-made layup through a mold, that was designed in 3D CAD/CAM and was built in FRP.

In accordance to [19], the model hull tolerances for breadth, drought, and length are ±0.5 mm. The manufacturing tolerance for length is less than 0.05%, and special attention was paid into the shaping of chines and step.

2.2. Laboratory instrumentation and measurements

The calm water experiments were conducted in the towing tank of the University of Napoli, Federico II (Italy). The main dimensions of the basin are: length 137.5 m, width 9 m, depth 4.25 m.

The details on the laboratory instrumentation employed in the experimental tests and on the measurement techniques are reported in Appendix A.

A peculiar feature of the proposed EFD tests are represented by the wetted surface measurements. This have been possible through a video camera placed on towing carriage, in perpendicular position with respect to the model's center of gravity. The video camera with 50 mm lens recorded each test from the start to the end. In such a way, it has been possible to reconstruct the dynamic of the vortex phenomena near the step [20].

2.3. Test procedure

The model was tested in calm water, in accordance to [21]. The minimum time between two consecutive runs was 10 min, and each run was initialized with the recording of zero levels for each transducer. The resistance tests were conducted for a displacement condition of 30.705 N at zero trim and at eight different speeds: 1.290, 2.357, 3.131, 4.631, 5.368, 6.340, 7.301, and 8.050 m/s, (see Appendix B, Table A5).

The quantities measured are speed, resistance, sinkage, and trim angle. Digital photographs and videos for each run were acquired to determine the dynamic wetted surface and the vortical flow under the hull near the step.

The resistance dynamometer had been placed on the towing carriage and connected to the model through a wire to measure the resistance.

The calm water resistance experiments were conducted with "down-thrust" (DT) methodology proposed in [22] with a towed point located in the hull bow (see also Fig. 2). The choice of the

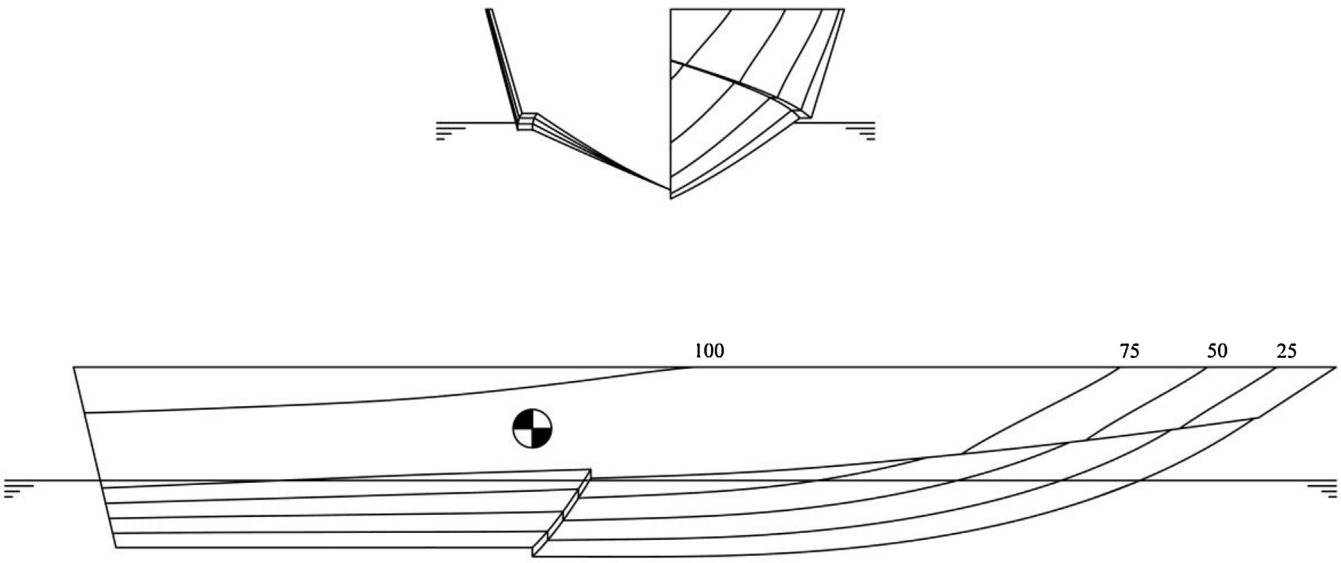

Fig. 1. C03 model body plan (transversal section every 0.100 m) and profile (buttock line every 0.025 m).

Fig. 2. Towing tank test with down-thrust methodology.

DT measurement solution is due to the high sensitivity of the hull model to the external applied forces, *i.e.*, instrumentation weight. The DT solution releases the tested model from the instrumentation weight and promotes higher accuracy in measurements of resistance, sinkage, and trim. This solution has proven to reproduce the real system of forces exerted by the outboard engines.

2.4. EFD results and uncertainty analysis

The results of calm water resistance tests are presented in Figs. 3–6, and Table 2. All values are plotted against volumetric Froude number (Fr_∇). In particular, the nondimensional total resistance (R_{TM}/Δ) is shown in Fig. 3; the dynamic trim angle (τ) is shown in Fig. 4; the nondimensional dynamic sinkage ($Z/\nabla^{1/3}$)

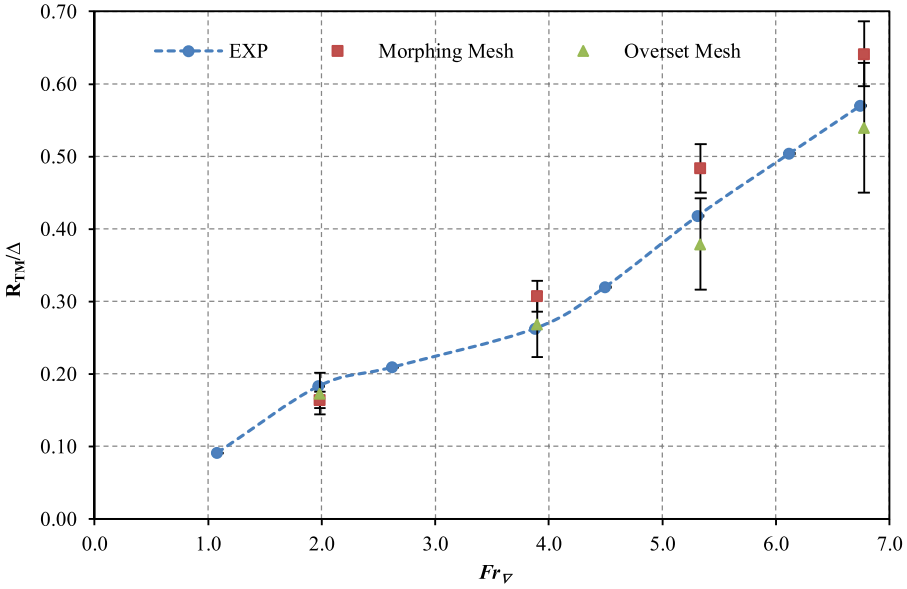

Fig. 3. Nondimensional total resistance comparison between EFD and CFD simulations with uncertainty bars.

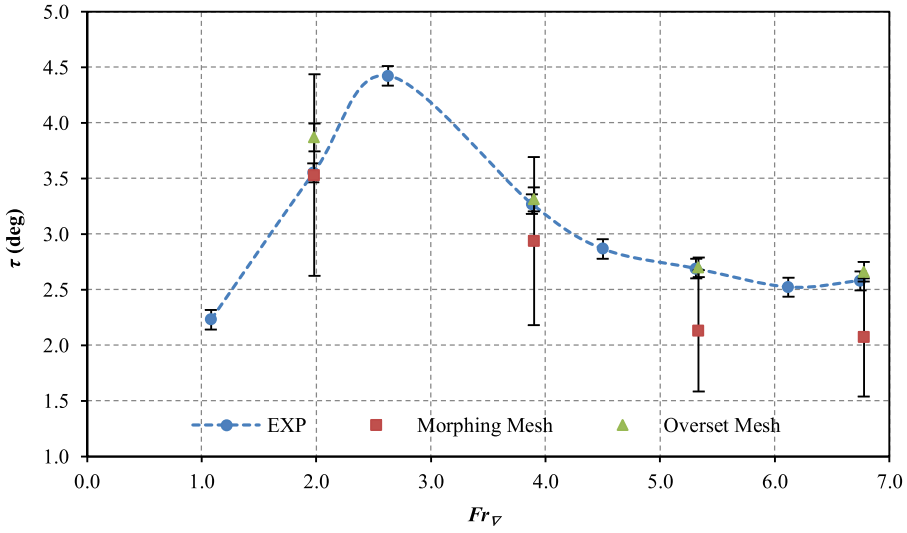

Fig. 4. Trim comparison between EFD and CFD simulations with uncertainty bars.

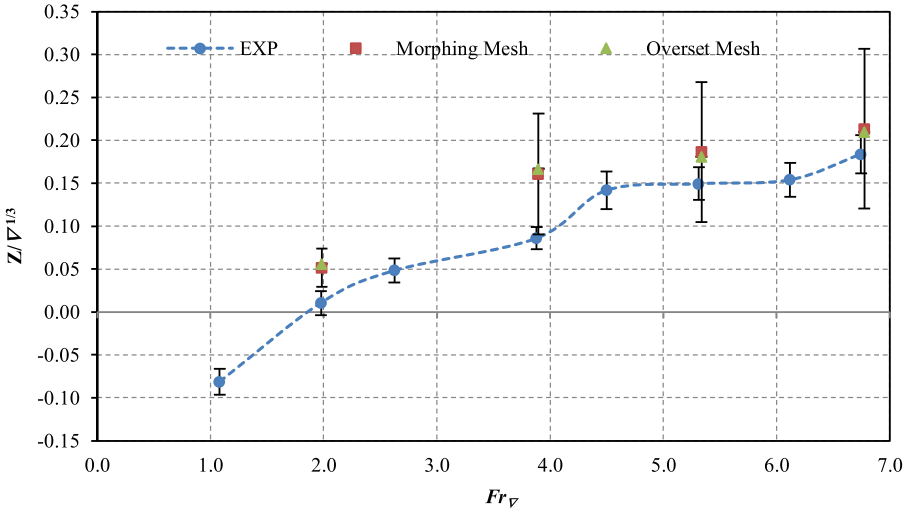

Fig. 5. Nondimensional dynamic sinkage comparison between EFD and CFD simulations with uncertainty bars.

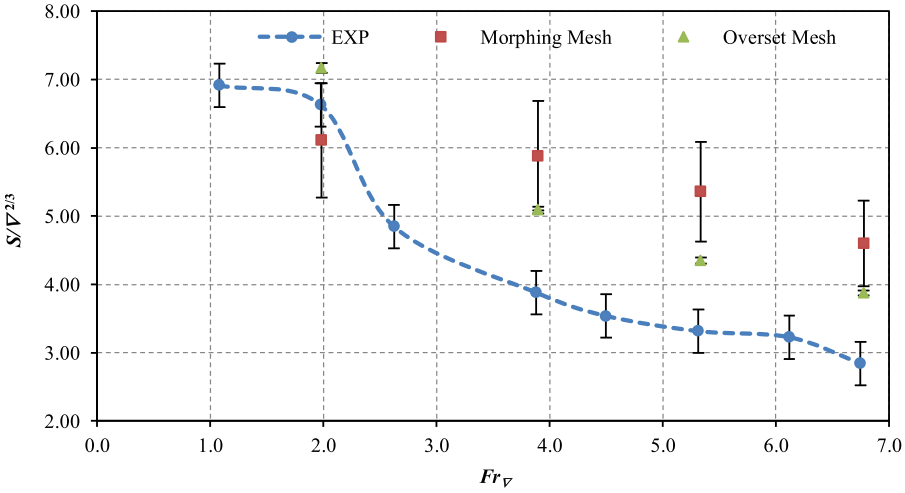

Fig. 6. Nondimensional dynamic wetted surface comparison between EFD and CFD simulations with uncertainty bars.

Table 2
Experimental and simulation results.

Fr_∇	$\frac{R_{TM}}{\Delta}$			τ			$\frac{Z}{\nabla^{1/3}}$			$\frac{S}{\nabla^{2/3}}$		
	Exp	CFD Morphing	CFD Overset	Exp	CFD Morphing	CFD Overset	Exp	CFD Morphing	CFD Overset	Exp	CFD Morphing	CFD Overset
1.984	0.183	0.164	0.173	3.55	3.53	3.87	0.011	0.051	0.056	6.631	6.110	7.171
3.898	0.263	0.307	0.268	3.27	2.94	3.31	0.086	0.161	0.167	3.881	5.885	5.092
5.337	0.418	0.484	0.379	2.69	2.13	2.70	0.149	0.186	0.181	3.316	5.358	4.349
6.777	0.570	0.642	0.540	2.58	2.07	2.66	0.184	0.213	0.210	2.845	4.601	3.873

is shown in Fig. 5; the nondimensional dynamic wetted surface ($S/\nabla^{2/3}$) is shown in Fig. 6.

These results are typical of a stepped hull. In particular, as expected, the trim angles are quite low for higher Froude numbers and change slightly with Fr_∇.

A significant outcome of the present experimental investigation is given by the observation of some clear vortical patterns that develop into the unwetted aft body area behind the step, and partly continue downstream in the water wake. The vortex in the unwetted aft body area appears for towing speeds greater than 2.36 m/s ($Fr_\nabla > 1.97$). These phenomena are visible thanks to the transparent bottom of the hull model, which was expressly designed. Some pictures of the flow patterns are shown in Fig. 14 (upper part), and Fig. 22 (upper part). Additionally, a video recording of a towing tank run has been released in the public domain [20]; it documents the time development of well visible vortex structures under the hull, as seen from an observer looking from the top and through the transparent bottom.

An Uncertainty Analysis (UA) of the EFD results has been also performed according to ITTC [23], as reported in Appendix B.

3. Numerical tests

In order to confirm the experimental results presented above, including the existence of the observed vortices, a campaign of CFD simulations has been devised. Moreover, a detailed study of the flow field has been made to reconstruct the vortex patterns both into the unwetted aft body area and in water downstream the step.

In this section, the details of the numerical setup used in all the simulations are reported. In particular, the detailed analysis of common and different setup used in the two different mesh approaches applied in this study are presented and discussed.

Unsteady RANS simulations were performed on four model speeds: 2.357, 4.631, 6.340, and 8.050 m/s, corresponding to Fr_∇ = 1.984, 3.898, 5.337, and 6.777.

3.1. Physical modeling and coordinate system

The unsteady Reynolds Averaged Navier Stokes (RANS) equations are solved using an implicit and iterative solver in order to find the field of all hydrodynamic unknown quantities in each time step. The velocity–pressure coupling and overall solution procedure were based on a semi-implicit method for pressure-linked equations (SIMPLE) to conjugate pressure and velocity fields. The discretized algebraic equations were solved using a point-wise Gauss–Seidel iterative algorithm and an algebraic multigrid (AMG) method was employed to accelerate solution convergence. Furthermore, a segregated flow solver approach was used for all simulations and the turbulence closure of the RANS equations was ensured by the k-ω shear stress transport (SST) turbulence model.

The RANS solver is based on a finite-volume method to discretize the physical domain. All the results presented in this study were achieved by solving the full unsteady flow equations and marching the numerical simulations in time with a pseudo-compressibility approach. The equations for the multiphase fluid are joined with one more transport equation for the VoF model. This equation helps to ensure the correct shape of the free surface between water and air. In these simulations, the modified high-resolution interface capturing scheme (HRIC) was used as advection schemes. The modified configuration of the HRIC scheme removes the dependency of the scheme on local Courant-Friedrichs-Lewy number (CFL), as reported in [24]. This correction is applied to avoid the common problem of free surface interface spread, also known as Numerical Ventilation (NV) [25] and [26]. This problem is one of the main

sources of error in the numerical simulations, in particular for planing hull resistance test simulations, as indicated by [27].

In order to simulate the hull free to move in the pitch and heave directions, the Dynamic Fluid Body Interaction (DFBI) model was used. The DFBI model allowed the RANS solver to evaluate the force and moments on the hull and to solve the governing equations of body motion in order to relocate the body. The DFBI model has been applied by using two different methods: the overset mesh method and the morphing grid.

The right-hand orthogonal coordinate system *O-XYZ*, as used in all simulations, has the origin of the reference frame located in the longitudinal position of the center of buoyancy (LCB) (*X* coordinate), in the vertical position of the calm free surface (*Z* coordinate), and transversal position in the symmetry plane (*Y* coordinate). The positive *x*-axis is forward oriented and parallel to the baseline of the hull, the positive *y*-axis points to portside, and the positive *z*-axis points m vertically upward.

A CFD code commercially available, STAR-CCM+ by CD Adapco, was used for mesh generations and computations.

3.1.1. Computational domain and time-step analysis

As for the computational domain, the boundaries were placed far enough away from the ship hull in order to avoid the well known problem of fluid flow reflection. The overset mesh technique required two different regions, *i.e.*, the background and overset regions, as shown in Fig. 7 (a). It is important to note that in the ship hydrodynamics field no defined recommendations in terms of domain dimensions are available for the overset region, as indicated in [28]. However, the dimensions of the background region were chosen in compliance with the ITTC's CFD recommendations [29], in particular the dimensions were set to more than twice of the values recommended by the ITTC.

In regards to the morphing mesh approach, only one region was required, and the relevant dimensions of the calculation domains were in compliance with the ITTC prescriptions [29] (in particular the dimensions were not less than 2.5 times the ITTC recommendations), as shown in Fig. 7(b).

The dimensions of the calculation domains and the boundary conditions for the two different mesh approaches are illustrated, respectively, in Figs. 8–11

The flow around the ship hull was assumed symmetrical with respect to the center plane. This is a typical boundary condition used in the CFD resistance test simulations, as indicated in the ITTC guidelines [29], and the effects of this assumption are negligible in terms of simulation results, as indicated in many works. This is a reasonable assumption that leads to significant reduction in terms of computational time (see Fig. 10).

The time-step used in the simulations is a function of the hull speed, according to the following ITTC equation [29]:

$$\Delta t = 0.01 \sim 0.005 \frac{l}{V} \tag{1}$$

where V is the hull speed and l is the length characteristic value of the analysed body. In this study, l was assumed equal to the dynamic L_{WL}, detected by towing tank tests at each analysed speed. Furthermore, the time-step is also a function of the grid density when, as in this case, the CFL number has to be kept constant.

A summary of the main properties of the numerical solver used for the overset and morphing mesh cases are reported in Table 3.

3.2. Overset/chimera grid setup

One of the main advantages of the overset/chimera grid technique for the hull motion is that this approach ensures a good numerical accuracy near the far field boundaries. This is a typical problem occurring in planing hull simulations where there is a significant variation of the dynamic trim angle, as reported in [27].

Table 3
Summary of numerical simulation setup.

Pressure link	SIMPLE
Pressure	Standard
Convection Term	2nd Order
Temporal Discretization	1st Order
Time-step (s)	Function of velocity and grid
Iteration per time-step	5
Turbulence Model	k-ω SST

Table 4
Overset case: mesh properties summary.

Type of mesh	Trimmed (Background. Region)	Polyhedral (Overset Region)
No. of cells	662290	1994122
Base size (m)	0.3	0.7

However, the simulations performed with the overset/chimera grid method require additional settings. In particular, to establish the connectivity between the background and the overset regions, an interpolation scheme is required. According to previous numerical tests conducted on planing hull models [30], it has been identified that the linear interpolation scheme is the most suitable in terms of adequacy of the numerical results with the experimental data. However, the computational effort required is higher with respect to the other methods. A detailed analysis of the different interpolation schemes available with the overset/chimera grid method are reported in [14].

The overset mesh solution for this analysis is similar to the solution adopted in [31] with trimmed mesh (background region) and polyhedral mesh embedded zone (overset region), as shown in Fig. 7(a). The main data of the mesh solution chosen for the background and overset regions are given in Table 4.

The dimensions of the calculation domains and the boundary conditions are illustrated in Fig. 8 and Fig. 10.

3.3. Morphing mesh grid setup

It is known that morphing grids require special treatment of the moving nodes in order to control the accuracy of the space derivatives and of the time-stepping scheme. This is done by appropriately interpolating the fluid flow variables. Then, the interpolation field is used to displace the vertices of the mesh based on the Radial Basis Functions (RBF) method. To generate the interpolation field, a system of equations is solved, using the control vertices and their specified displacements: for every control vertex i, its displacement d_i' is approximated by the combination:

$$d_i' = \sum_{j=1}^{n} \lambda_j \sqrt{r_{ij}^2 + c_j^2} + \alpha, \tag{2}$$

where $r_{ij} = |x_i - x_j|$ is the magnitude of the distance between two vertices, λ_j is the expansion coefficient, x_i the position of i-vertex, n is the number of control vertices, c_j the basis constant, and α a constant value. More details are reported in [32].

Differently from what happens for the overset/chimera grid method, the morphing grid does not require additional settings. The dimensions of the calculation domain and the boundary conditions are illustrated in Figs. 9 and 11, respectively.

In the simulations presented in Section 4 (see Fig. 3–6), the morphing technique is combined with rigid motions, as mentioned above. As morphing strategies can lead to poor quality cells, it becomes important to keep under control the topological deformations taking place in the surface mesh and in the volume cells, by

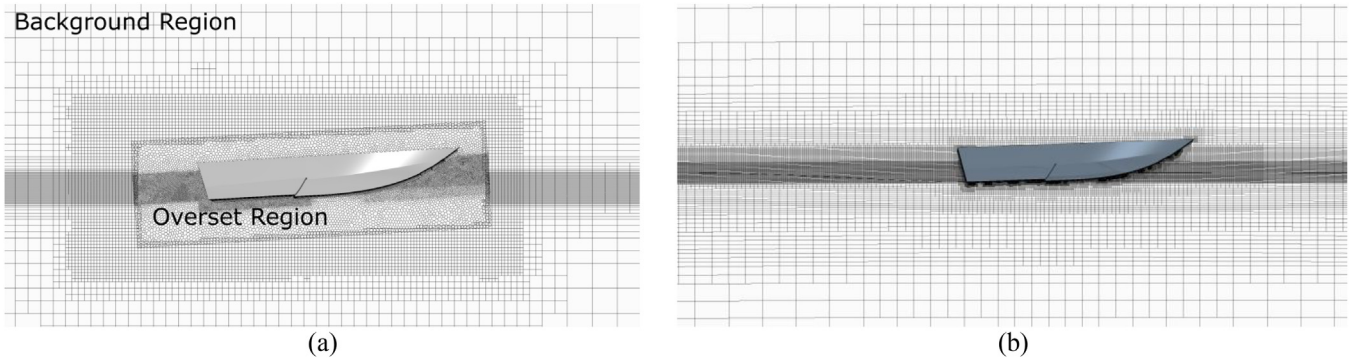

Fig. 7. (a) Overset grid visualization with different meshes for regions (polyhedral: overset region, trimmed: background region): (b) morphing mesh visualization.

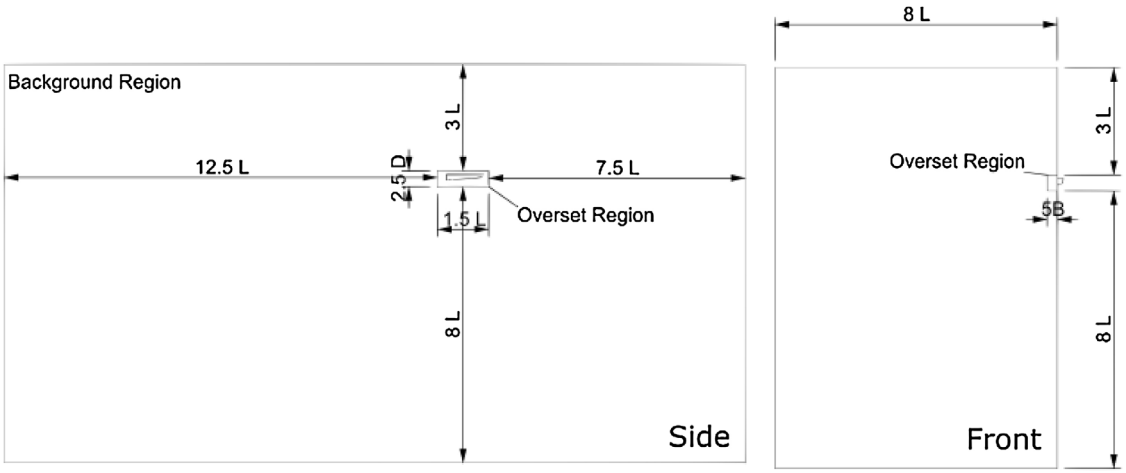

Fig. 8. Domain dimensions: overset grid case.

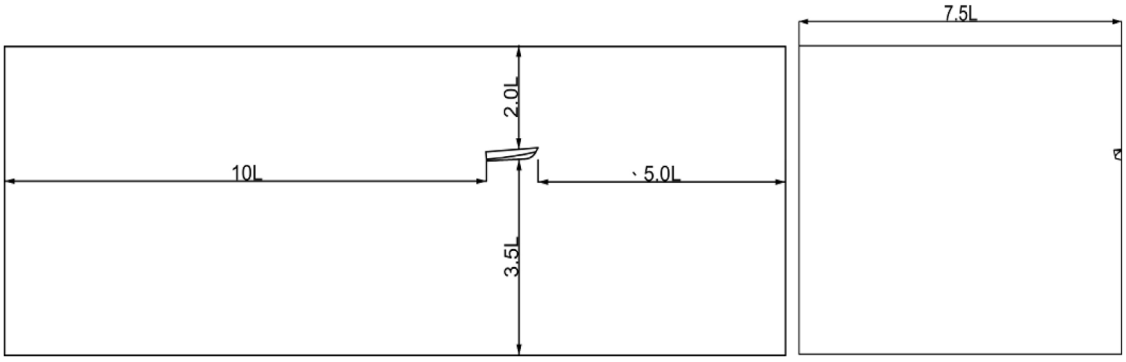

Fig. 9. Domain dimensions: morphing grid case and LES simulation.

means of specific mesh quality metrics. To minimize the topological deformations of the grid domain, the hull at the starting point has an initial trim angle of 2 ° aft.

A visualization of the grid with refinement in the air/water interface area is shown in Fig. 7(b).

3.4. Wall y+ treatment

The wall function was used for the near wall treatment, and the *All-Wall y+* [14] is the wall treatment used for all simulations. It is a hybrid approach that attempts to emulate the high *y+* wall treatment for coarse meshes (for $y+>30$), and the low *y+* wall treatment for fine meshes (for $y+\approx 1$). It is also formulated with the desirable characteristic of producing reasonable answers for meshes of intermediate resolution (for *y+* in the *buffer layer*), [14]. This approach is considered a reasonable compromise among the acceptable quality of the boundary layer description and the calculation time. The values of wall *y+* near the hull are shown in Fig. 12, where it is possible to observe the wall *y+* range on the hull at maximum speed tested for the two different mesh techniques.

3.5. Verification and validation study

A verification and validation study (V&V) is conducted for R_{TM}/Δ, τ, $Z/\nabla^{1/3}$, and $S/\nabla^{2/3}$ at one speed (4.631 m/s, $Fr_{\nabla}=3.898$). The results of this analysis are reported in Appendix C.

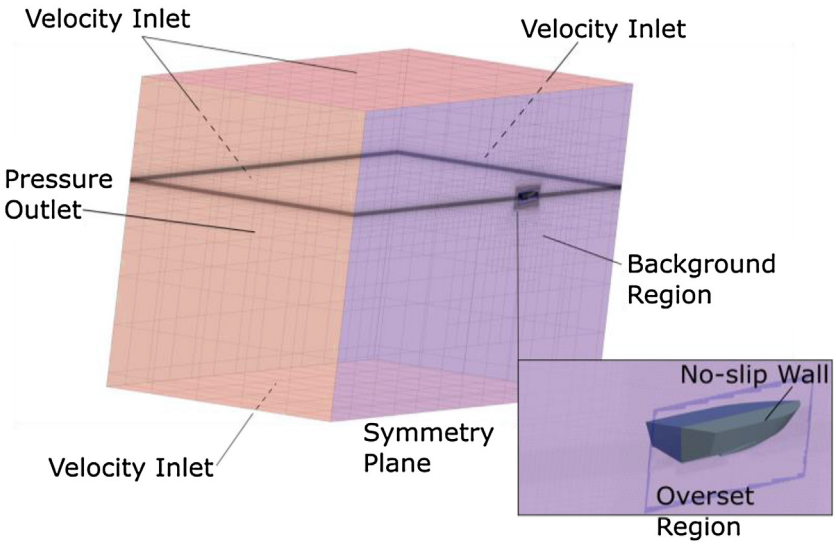

Fig. 10. Boundary conditions: overset grid case (view from the back of the domain).

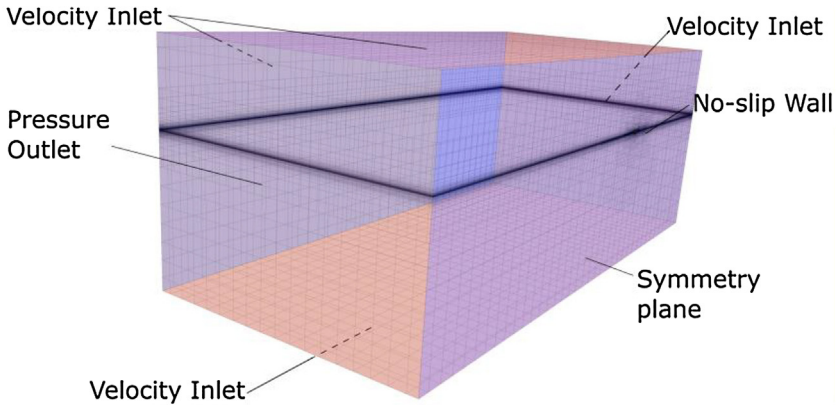

Fig. 11. Boundary conditions: morphing grid case (view from the back of the domain).

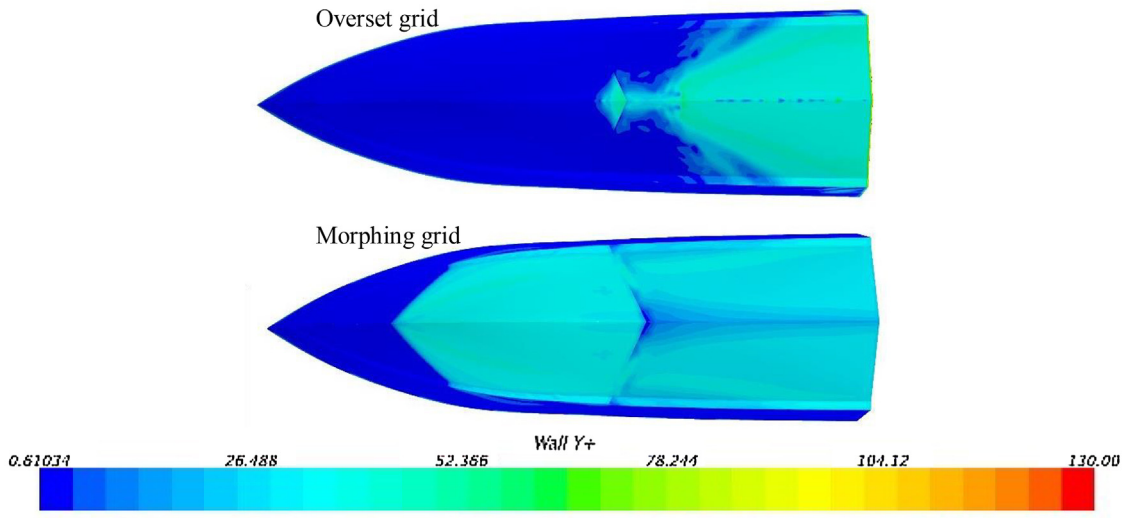

Fig. 12. Wall y+ visualization on the hull at $Fr_\nabla = 3.898$ for the different mesh technique: overset/chimera grid (top), morphing grid (down).

The V&V study results and the uncertainty analysis for the two different simulation techniques , *i.e.*, overset and morphing mesh, are listed in Table A6 and A7, respectively.

The monotonic convergence is reached in all cases except for the sinkage in the overset mesh. The validation process is achieved for the resistance/displacement ratio and for the trim angle in the overset case. In spite of what happens with the overset mesh, for the

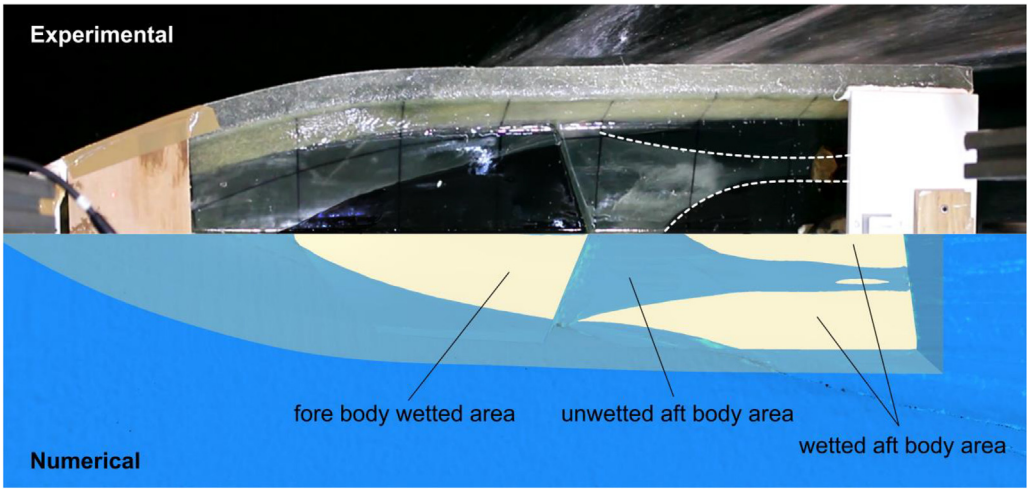

Fig. 13. Wetted surface top view at $Fr_\nabla = 3.898$, comparison between experimental (top side), and RANSE overset simulation 2.5×10^6 cells (down side), air/water interface as isosurface at VoF = 0.5.

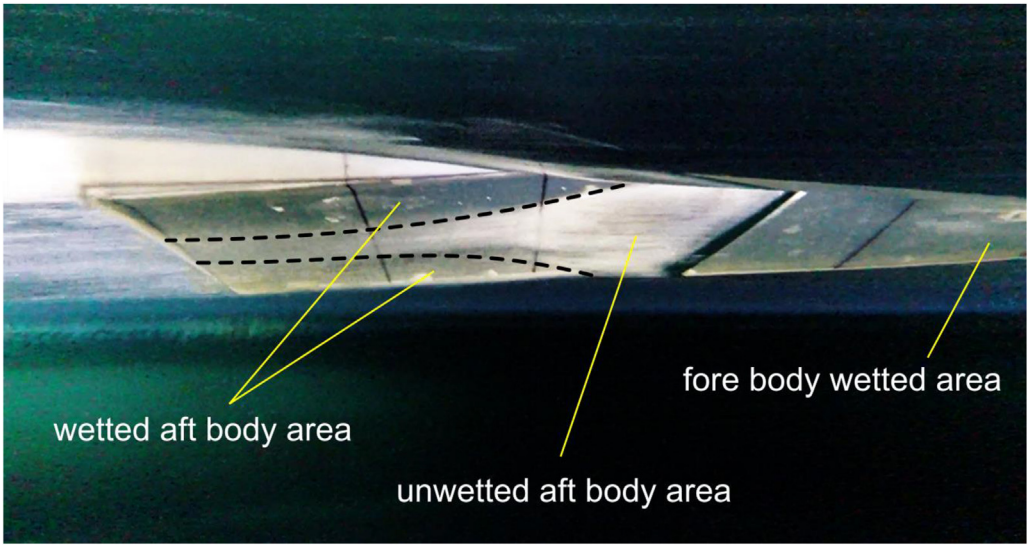

Fig. 14. Experimental wetted surface right-side view at $Fr_\nabla = 3.898$.

morphing mesh case a higher scatter in the solutions is detected. This is probably one of the main reasons for which the validation is achieved only for the sinkage and trim angle. When the comparison error is much higher than validation uncertainty ($E \gg U_V$), in particular for the wetted surface, the validation is not achieved, but it is significant, and the main challenge becomes the improvement of the simulation modeling.

The iterative uncertainty is not reported in the tables above because it was found to be always negligible with respect to other sources of uncertainty, as shown in similar studies, e.g. [29].

4. Results and discussions

In this section, a comparison between experimental and numerical results is presented and discussed.

The main aims are to evaluate the reliability of the different simulation techniques adopted, as well as to find a confirmation in the numerical simulations of the vortex phenomena observed experimentally in the aft body waterplane area behind the step.

Secondly, the numerical analysis is used to reconstruct with greater detail the recirculation paths, which are seen experimentally from top- and side-view photographs.

The results in terms of R_{TM}/Δ, τ, $Z/\nabla^{1/3}$, and $S/\nabla^{2/3}$ versus Fr_∇ are reported in Figs. 3–6, respectively.

4.1. Total resistance, dynamic sinkage, and trim angle

The numerical results are in accordance with the experimental data and all of the experimental and numerical results are summarized in Table 2. The better performance of the overset grid approach is evident because, as compared with the experimental

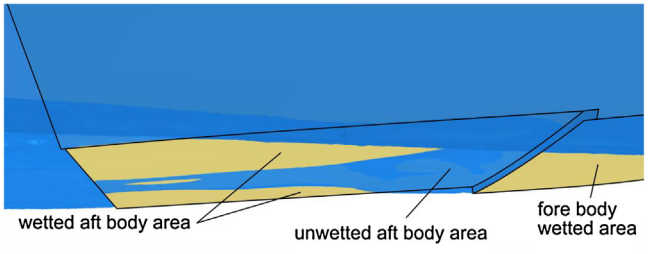

Fig. 15. Wetted surface right-side view at $Fr_\nabla = 3.898$, RANSE overset simulation (2.5×10^6 cells), air/water interface as isosurface at VoF = 0.5.

values, the percentage differences are in the range from 2.2% to 9.3% for the R_{TM}/Δ.

Similar results are achieved for trim angle, in particular for the velocities greater than the hump speed (3.13 m/s, 2.61 Fr_∇), the overset grid has better performance respect to the morphing grid approach when compared with experimental values. The difference between the two methods is mainly due to the underestimation of trim with morphing grid for velocities greater than the hump speed, as shown in Fig. 4.

The value of the numerical nondimensional dynamic sinkage with the two different mesh techniques are closer and the percentage differences, comparing the overset approach and morphing grid, are up to 8.9%, as shown in Fig. 5.

However, the overset mesh technique is more effective than the morphing technique, but more demanding in terms of computational times required (1800 versus 980 s of CPU time per time step).

4.2. Dynamic wetted surface

The amount of wetted surface area reduction is not directly related to the drag reduction as pointed out by Amromin [33]. However in this section, for the sake of completeness, the process of dynamic wetted surface calculation is discussed.

Fig. 6 shows a comparison between numerical and experimental values of the $S/\nabla^{2/3}$ versus Fr_∇. The experimental wetted surface

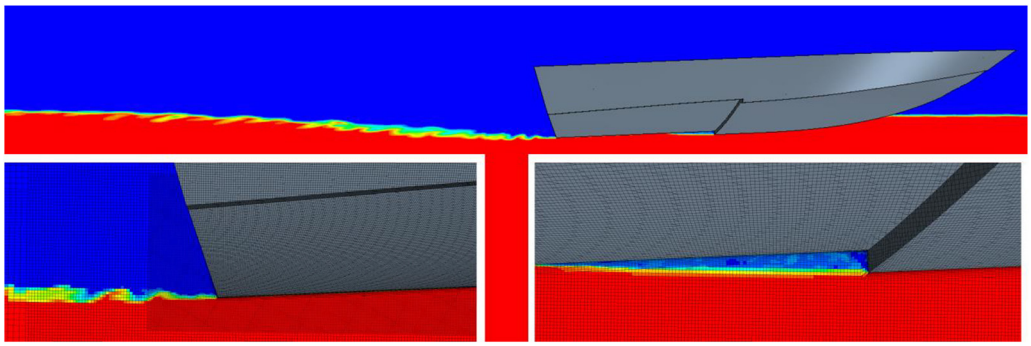

Fig. 16. Details of the LES simulation at $Fr_\nabla = 3.898$ with very fine grid used for the flow pattern study in the unwetted aft body area (12×10^6 cells). Contour maps of VoF (red in water; blue in air). See also Fig. 19. (For interpretation of the references to colour in this figure legend, the reader is referred to the web version of this article.)

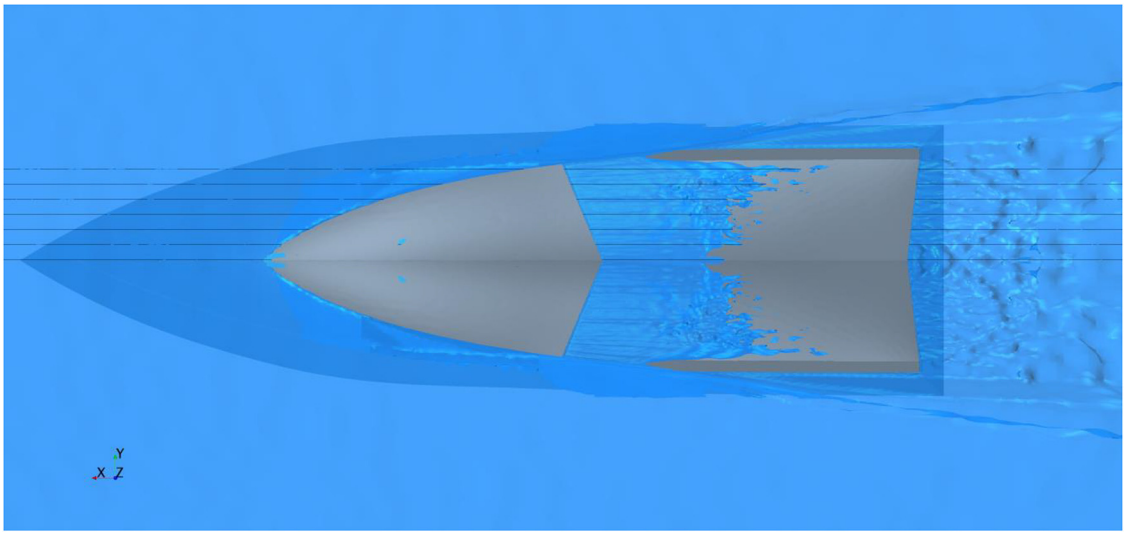

Fig. 17. LES simulation; bottom view at $Fr_\nabla = 3.898$ with VoF isosurface at 0.5, and wave cuts (12×10^6 cells).

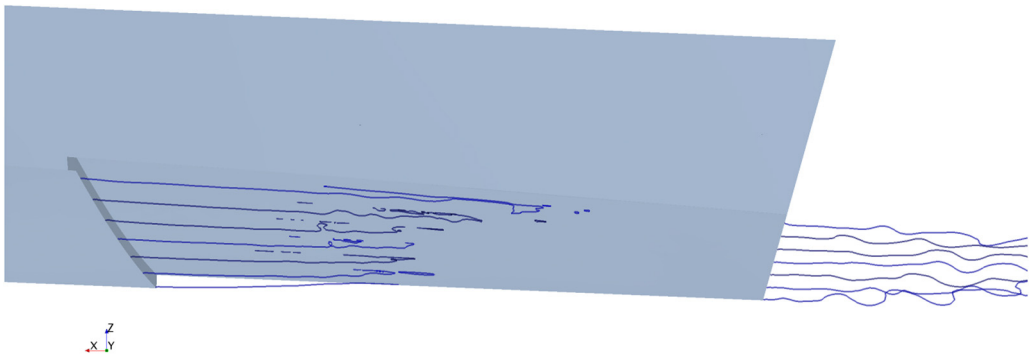

Fig. 18. LES simulation; side view at $Fr_\nabla = 3.898$ of wave cuts of VoF isosurface at 0.5, dry region behind the step and stern wake profile.

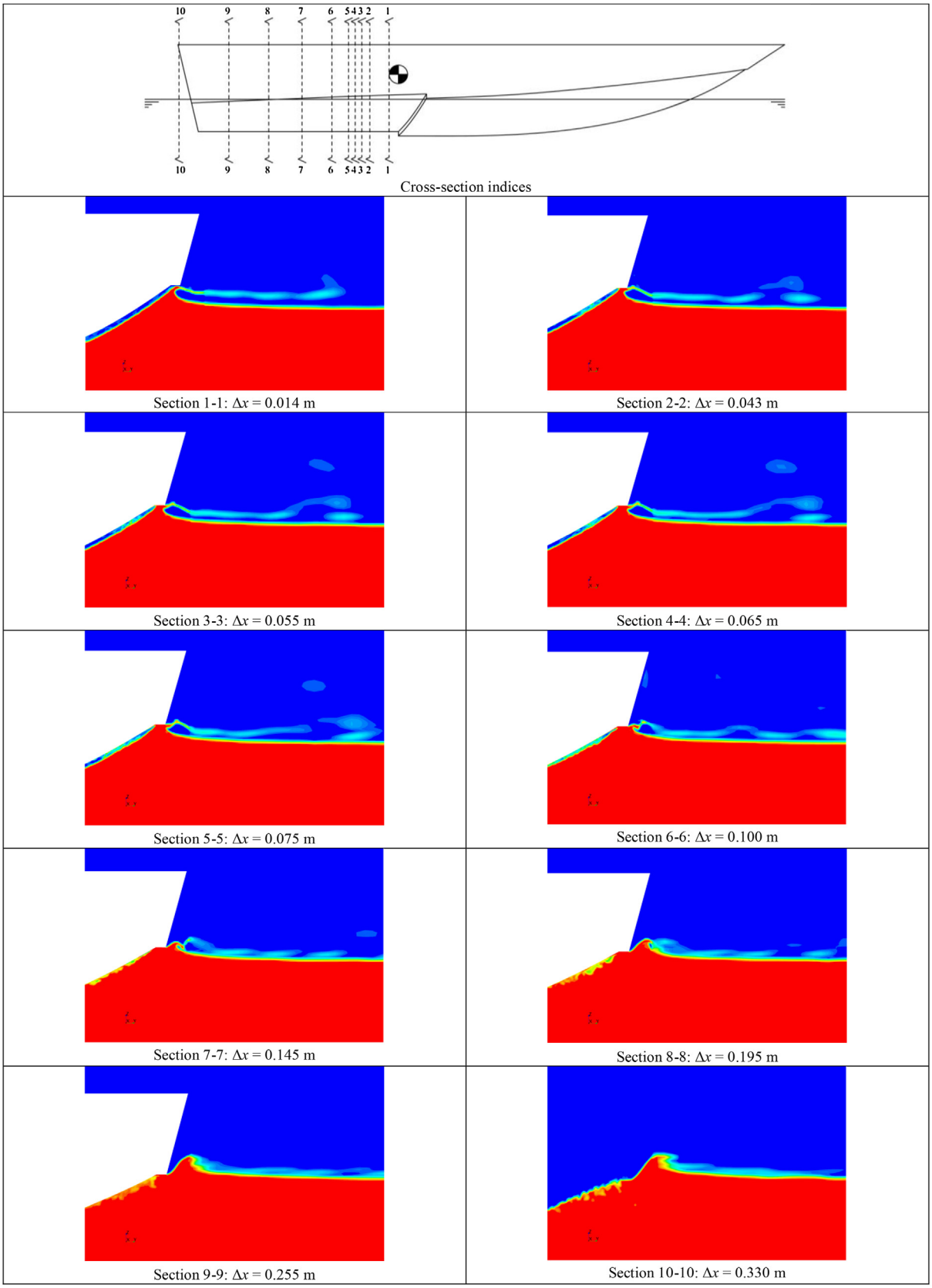

Fig. 19. LES simulation; volume fraction contours at different cross sections (at Δx from LCB, positive forward), at $Fr_{\nabla} = 3.898$. Contour maps of VOF (red in water; blue in air). (For interpretation of the references to colour in this figure legend, the reader is referred to the web version of this article.)

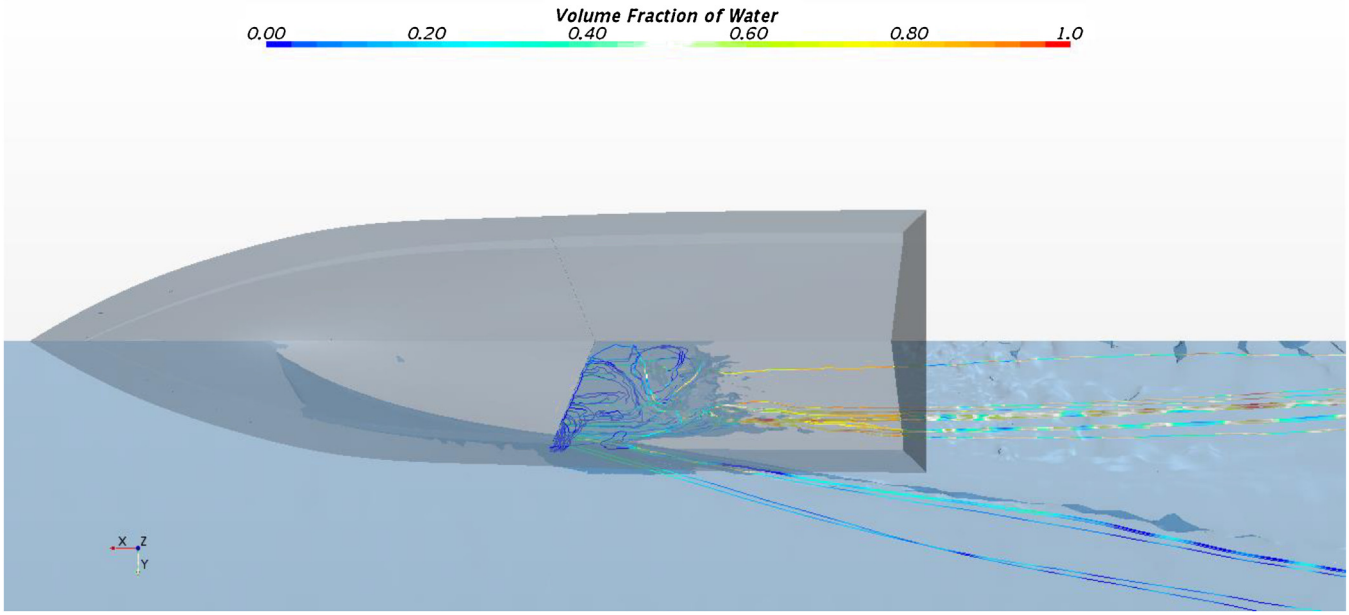

Fig. 20. LES simulation; streamlines in air and water at $Fr_\nabla = 3.898$.

values are estimated through digital analysis of video frames, which are referenced to the original 3D CAD model. On the other hand, the numerical values are calculated by the fluid dynamics solver. In general, especially at high Froude Numbers, the values of wetted surface calculated numerically are more reliable than those extracted from the video recordings.

A source of uncertainty in the estimation of wetted surface is the spray area, which is difficult to evaluate experimentally on the basis of the video footages. In fact, as reported in Appendix B, the bias of $S/\nabla^{2/3}$ is mainly composed by the bias of wetted surface estimation (B_S), which is 80.81% of $S/\nabla^{2/3}$ total bias.

The issue of evaluation of the spray area also affects the numerical solution; indeed, this evaluation is a nontrivial task for RANS solvers and requires a very high-resolution grid, as indicated in [34]. For this reason, the overestimation of the wetted surface with respect to the experimental results is due to the use of a VoF threshold value equal to 0.5 as indicated in [29].

The numerical results are closer to the experimental measurements when obtained with the overset mesh approach, as opposed to the morphing grid approach. The difference between the two numerical methods is mainly due to the underestimation of trim, as shown in Fig. 4.

In particular, the experimental wetted surface amount is underestimated with respect to the real wetted surface, but the numerically estimated wetted surface overestimates the real wetted surface due to the chosen VoF value threshold. Consequently the real wetted surface values can be considered located between experimental and numerical (overset mesh) values.

As mentioned above, the use of the transparent bottom hull was provided to ensure a full view of the water flow under the hull and a more effective estimation of S. During the towing tank tests, a particular flow phenomenon was detected at all Fr_∇. This phenomenon consists in two vortex structures under the hull and behind the step, as shown in the video footage [20].

However, for this study the speed condition of $Fr_\nabla = 3.898$ was chosen because the phenomenon is especially well visible (see Figs. 13 and 14).

The vortex structures are also visible in the numerical simulations with an overset mesh approach, as shown in the two views of the flow under the hull (Fig. 13). The upper picture is a top view of the transparent hull model, showing the unwetted aft body area and a well-developed vortex. This vortex trails downstream into the water, departing from the aft region of the unwetted aft body area. The lower picture is taken from the numerical solution and shows the isosurface at VoF = 0.5. This visualization emphasizes the presence of the unwetted aft body area behind the step, as opposed to the fore body wetted surface. The two visualizations are in good agreement, both in terms of wetted surface extension and in terms of shape of unwetted aft body area.

Similarly, Figs. 14 and 15 show two side views of the underwater flow behind the step. Also in this case, the two visualizations show a good agreement between the experimental evidence and the numerical results.

4.3. Analysis of the fluid-dynamics in the unwetted aft body area

A detailed study of the flow patterns in the unwetted aft body area behind the step has been performed at $Fr_\nabla = 3.898$. Starting from the experimental values of trim and sinkage in this condition (see Figs. 4 and 5), the zero (DoF) hull has been simulated at the given Froude number with a large eddy simulation (LES) approach on a very fine grid of approximately 12×10^6 cells (see Fig. 16) with the same size of computational domain and boundary conditions previously described for the morphing grid simulation (see [14] for the details of the applied LES formulation). Successively, the converged solution has been used as the initial condition of further simulations with free heave-and-pitch degrees-of-freedom. The final two-DoF converged solution has been post-processed to gain insight into the complex flow pattern behind the step. The streamlines both in water and in air were analyzed, and a flow pattern in the unwetted aft body area was characterized. The flow patterns (in-air and in-water) are clearly visible from the bottom and side views of the LES solution shown in Figs. 17 and 18, and Figs. 20–24.

A bottom view of the LES solution is shown in Fig. 17 where some selected streamlines on the air/water interface have been calculated and visualized. The same streamlines are visible in Fig. 18. These representations emphasize the shape of the unwetted aft body area and the extension in the aft region of the step. In particular, the extension of the separated region is evident from the flow

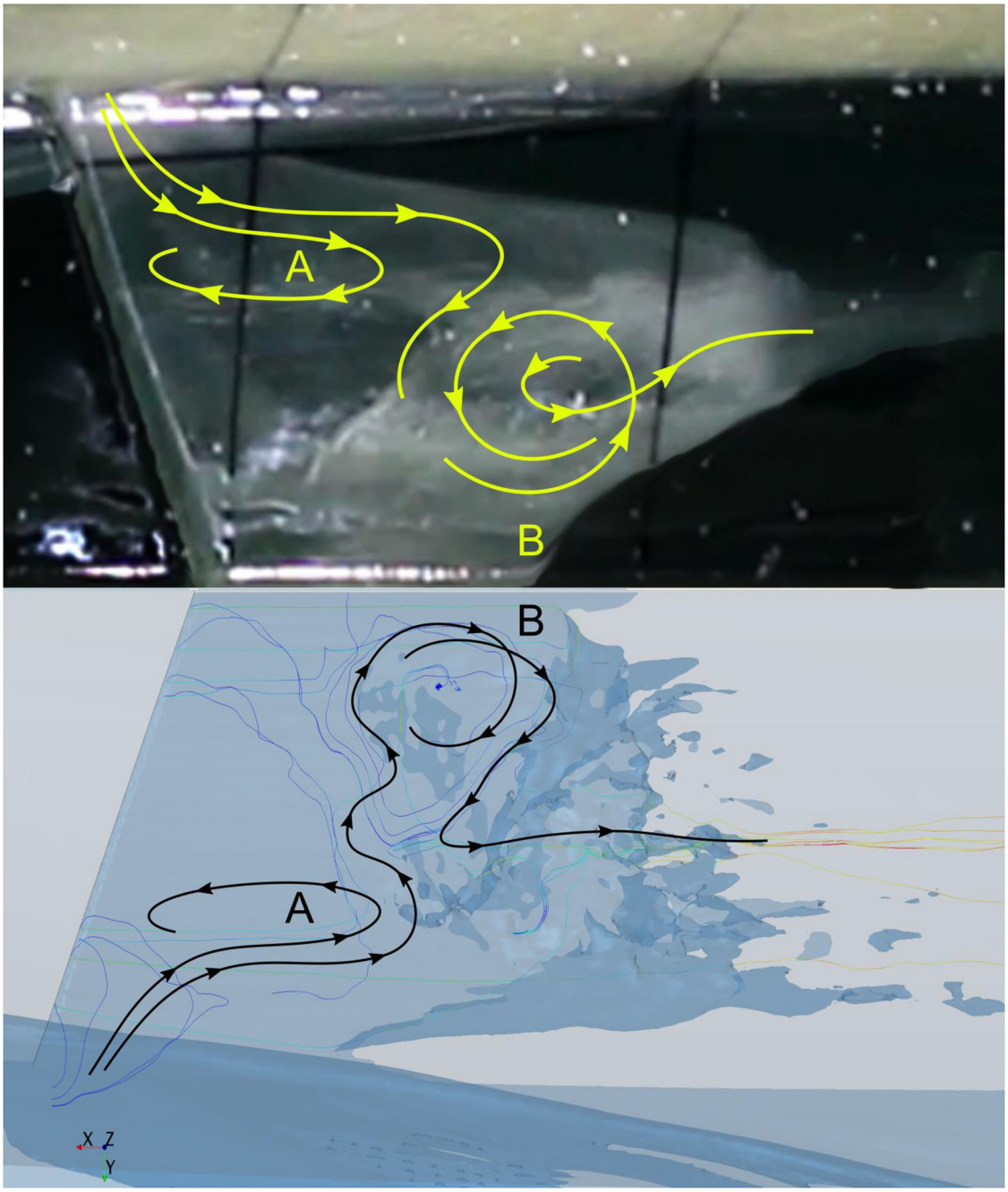

Fig. 21. LES simulation; flow patterns in the unwetted aft body area, top view at $Fr_{\nabla} = 3.898$.

field cross sections of Fig. 19 at different x-stations ($x = 0$ at the LCB, Fig. 1).

A more detailed set of visualizations is given by Figs. 20–22. The main feature of the flow pattern inside the unwetted aft body area depends on the air inlet (shape and longitudinal position). The air inlet is located at the intersection of the chine with the step, and facing the side of the main flow. A fairly complex 3D flow is visible from the representation of the streamlines. The air particles enter the unwetted area through the inlet and successively propagate inside the air region according to different patterns. Finally, a mix of air and (mostly) water particles flows downstream of the aft body into a visible vortex. The separation of the water-flow induced by the step is similar to what happens in the transom. The pressure of the flow after the separation is the atmospheric pressure. The physics of this 3D-phenomenon is mainly regulated by the Fr_{∇} according to [1]. Therefore, according to [7] the cavitation number behind the step is $\sigma = 0.018$.

A close-up picture of the transparent hull model taken from the experimental test is shown in Fig. 21 (upper part). In the photograph, the two-main observed counter-rotating flow patterns are depicted and named *pattern A* and *pattern B*. In the lower part of the same figure, a similar visualization taken from the LES solution is reported. Two similar flow patterns are visible by inspection of the numerically calculated streamlines. The complexity of the 3D streamlines is visible in Figs. 22 and 23. The side view of Fig. 23 shows that streamlines originating from the inlet propagate according to a recirculating path induced by the external water flow overcoming the step. Finally, a perspective bottom view of the streamlines is shown in Fig. 24.

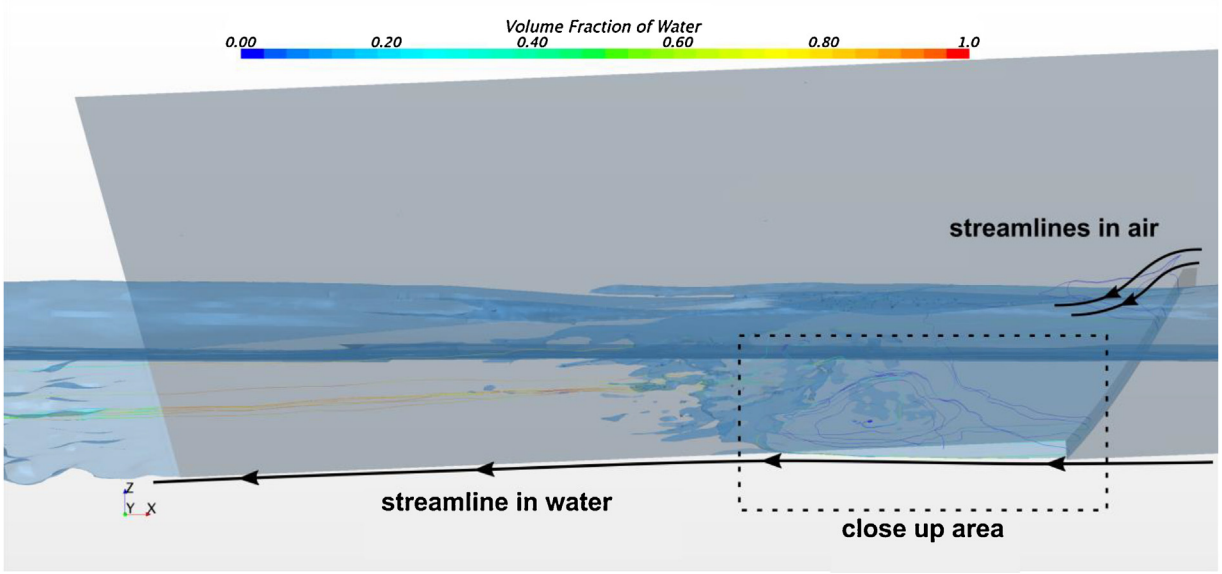

Fig. 22. LES simulation; side air inlet at the step, side view at $Fr_\nabla = 3.898$.

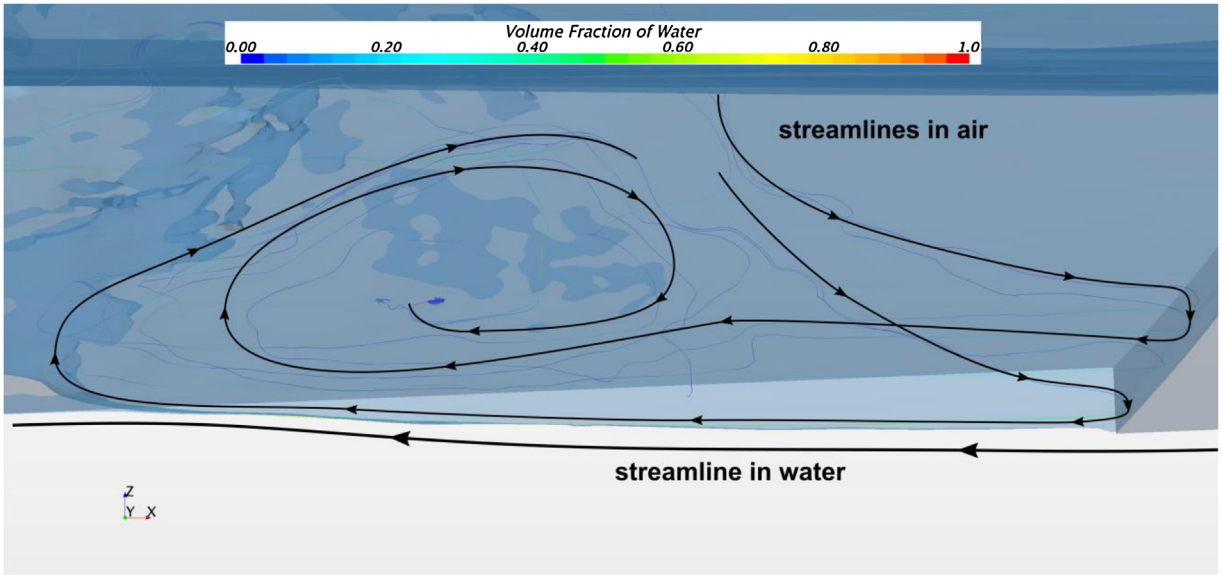

Fig. 23. LES simulation; close up of 3D patterns of air flow in the unwetted aft body area, side view at $Fr_\nabla = 3.898$.

The flow patterns obtained numerically look similar to the ones observed in towing tank investigations. The same flow patterns seem to be confirmed by ongoing LES simulations on a full scale hull with a very fine grid of 17.7×10^6 cells. The LES simulation has been performed for a speed of 15.5 m/s, (28.5 knots in full scale), equal to $Fr_\nabla = 3.898$. Furthermore, the results in terms of trim angle, and nondimensional total resistance, sinkage, wetted surface, are comparable with respect to the model scale simulation.

5. Conclusions

Calm water resistance experiments have been conducted on a single-step hull model with a transparent bottom in order to study the vortical flow phenomena featured by this type of planing hulls. An uncertainty analysis of the experimental results has been performed in compliance with the ITTC standards.

Due to the hull model's low weight and sensitivity to external applied forces, the "down-thrust" methodology was applied in order to release the model from the instrumentation weight. This approach allowed high precision of data acquisition, i.e. resistance, sinkage, trim, and dynamic wetted surface measurements. The proposed solution has proven to reproduce with good accuracy the real system of forces exerted by the outboard engines on the transom of the hull in full scale.

The transparent bottom of the hull model allowed the observation of some unique vortical flow phenomena in the unwetted aft body area behind the step. The vortex in the unwetted area appears for towing speeds greater than 2.36 m/s ($Fr_\nabla > 1.97$). Towing tank tests revealed that the flow in the unwetted aft body area is dominated by a rather complex 3D arrangement of vortices originating from air spillage at both sides of the step. On each side of the unwetted aft body area, one of the vortices inside the air bubble terminates at the air/water interface and develops into a trailing vortex in the water wake.

To confirm this experimental evidence, the same test conditions were reproduced with CFD simulations by using different

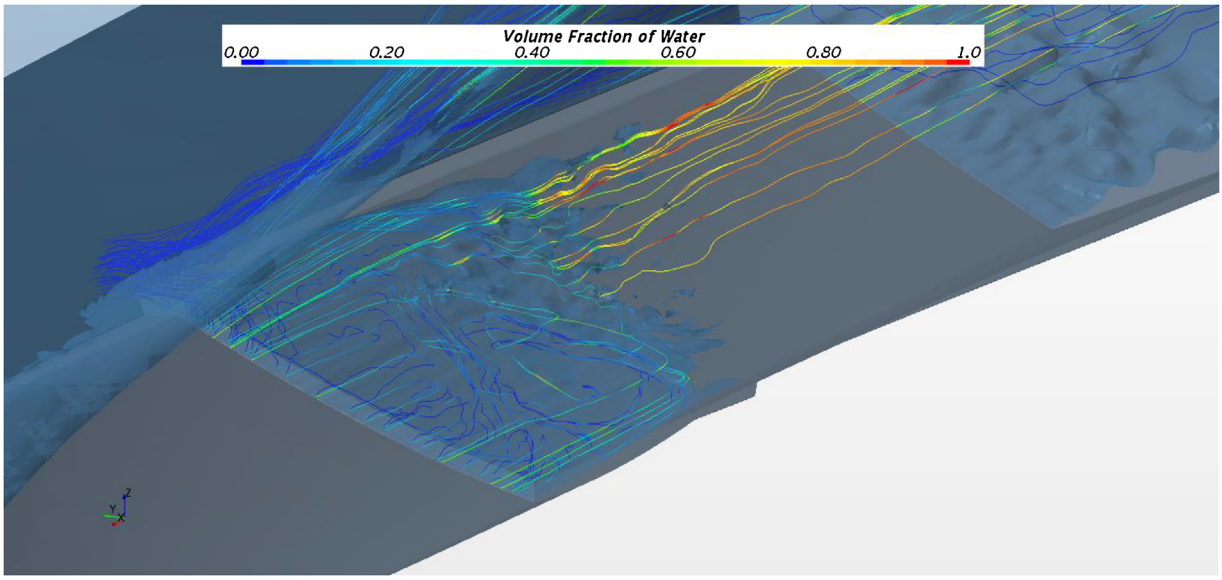

Fig. 24. LES simulation at $Fr_\nabla = 3.898$; perspective view of streamlines in the unwetted aft body area.

unconventional dynamic mesh techniques, *i.e.* overset mesh and morphing grid. The results of the overset mesh approach, in spite of being obtained with a greater computational effort, showed a better comparison error with respect to those of the morphing grid technique. The overset mesh ensures high-quality of the simulation results and shows high-adaptability to the wide variations of trim and heave of the stepped hull. As consequence, the numerical results, obtained by the overset mesh approach, are closer to the experimental measurements as opposed to the morphing grid approach, but more comprehensive studies are needed in order to improve the simulations and obtain high–fidelity results. In particular, a more in-depth evaluation of the grid approach, of the turbulence model effects, of the three-dimensional instability and surface tension effects is desirable.

The simulation uncertainty analysis has shown that the grid represents the main source of simulation numerical error, as already identified in another works. The uncertainty in the nondimensional variables (*i.e.*, total resistance/displacement ratio, nondimensional dynamic sinkage, dynamic trim angle, and nondimensional dynamic wetted surface) is, for the hull considered in this work, relatively greater when using the morphing grid technique. The validation process highlights that, in particular for the dimensionless wetted surface, the comparison error is much greater than the validation uncertainty, which implies that it is necessary to reduce the modeling error. However, by using LES approach on a refined grid, a detailed analysis of the flow in the unwetted aft body area behind the step shows that the results qualitatively matched the experiments and confirm the existence of the same vortical structures observed experimentally.

In summary, it can be said that about the simulation of stepped hull, the use of the overset mesh technique is suitable for the detection, in a sufficiently accurate way, of the total resistance and of the hull running attitude. Instead the LES approach is more suitable for the evaluation of the details of water flow phenomena around the hull and wetted surface. Moreover, in the design of planing/stepped hull, and in the absence of towing tank tests, a suitable approach is to couple RANS simulations, performed with the overset mesh technique, with LES simulations. The RANS can be used for the determination of the global parameters, *i.e.* resistance, trim and sinkage while the LES simulations can be reserved for any detailed investigations.

Furthermore, for the first time a particular vortex pattern in the unwetted aft body area has been observed for a scaled single-step hull model in towing tank tests. At the same time, similar flow patterns have been found in the numerical simulations on a very fine mesh, in which additional details on the 3D flow were explored in this area.

Acknowledgments

The authors are deeply grateful to the anonymous referees and to the editors for their suggestion and help in significantly improving the manuscript. They also deeply thank the HPC Centre SCoPE of University of Napoli “Federico II”, SCoPE academic staff for the given support, and towing tank staff as Mr Andrea Bove, Antonio Alfano, Biagio D’Abbusco, Lucio Iadicicco, and Vitale Esposito.

This work has been supported by: SIRena project grant (CUP C69F140000500008 – PON RC 2007/2013), ECO-RIB project grant (D.M. 01/06/2016 – Horizon 2020 – PON 2014/2020), and Mr. Vincenzo Nappo of the MV Marine S.r.l.

Appendix A. Laboratory instrumentation and measurement techniques

The tow carriage used in the towing tank of the Department of Industrial Engineering, Section of Naval Architecture and Marine Engineering, University Federico II of Naples is able to develop a maximum speed of 10 m/s with a maximum acceleration and deceleration of 1 m/s^2.

The carriage was instrumented on board with a sensor network and a Data-AcQuisition (DAQ) device. The sensors used in these tests are the encoder for speed carriage, load cell for resistance measure, balance for model and ballast weights, thermometer for water temperature, accelerometer for trim, and laser for sinkage.

The thermometer used during the tests allows a range −5 °C and 40 °C, with accuracy of 0.1 °C and resolution of 0.1 °C.

The speed of the carriage was measured by a high-quality encoder and a counter/timing card. The high-quality encoder rolls without rolling resistance driven by the carriage; it is not fixed to the any wheel drive of carriage, and it gives 1000 pulses per one round (1 pulse for each mm). The encoder sensor has an accuracy of 1 mm/m and a resolution of 1 mm. The period between two pulses was measured by a counter/timing card at 32 bits with a clock of

80 MHz. The card has a range from 1.25×10^{-8} s to 53.69 s; the clock at 80 MHz has an accuracy of $\pm 4 \times 10^{-3}$ MHz and a resolution of 1.25×10^{-8} s.

The resistance measure was performed by a high-quality load cell (precision class 0.003) and conditioning-acquisition card. The load cell has a range up to 50 N, an accuracy of 0.003%, and a resolution of 0.005 N. The conditioning-acquisition card has a software programmed range of 50 N, accuracy of 0.08%, 16-bit resolution, and sampling rate up to 200 kSamples/s. For these measurements, the row data were oversampled at a rate of 10 kSamples/s, and compressed at a rate of 500 Samples/s for ulterior reduction of the noise.

Running trim measure was performed by an accelerometer and a conditioning-acquisition card. The accelerometer sensor has a range of 40 m/s^2, accuracy of ±0.1%, and resolution virtually infinite. The conditioning-acquisition card has a software programmed range of 40 m/s^2, accuracy of 0.1%, and 16-bit resolution.

Sinkage was measured by two high-quality laser sensors and a conditioning-acquisition card. The two lasers have a range from 0.2 to 1 m, accuracy of 0.5 mm, and resolution of 0.05 mm. These laser devices were placed perpendicularly with respect to the water surface, at two positions, one at fore section and second at aft section. The conditioning-acquisition card has a software programmed range up to 1 m, accuracy 0.1%, and 16-bit resolution.

Weight of the model and ballast are measured with a balance with a range of 600 N, accuracy of ±0.1 N, and resolution of 0.1 N.

The calm water resistance experiments were conducted with "down-thrust" (DT) methodology proposed in [22] with a towed point located in the hull bow. This methodology considers that, in a horizontal position and in a trim angle at rest equal to zero, the direction of the towing force is applied in a point that is the intersection between the direction of thrust of engines and keel line at the bow. In the case of DT methodology, the model has 4Degrees of Freedom (DoF), with yaw and drift restricted. In fact, to avoid the instability phenomena, the model has been built with two guide model masts, one located in the bow and the other at the stern, which engages in two forks.

Appendix B. Experimental uncertainty analysis

Uncertainty Analysis (UA) in Experimental Fluid Dynamics (EFD) has been also performed according to ITTC [23]. As a first step, UA was performed for each individual variable r (model geometry, displacement, speed, resistance, density, running trim, and sinkage). Second, UA is performed for nondimensional coefficients (R_{TM}/Δ, τ, $Z/\nabla^{1/3}$, and $S/\nabla^{2/3}$). The UA procedure was based on the methodology proposed by [35] with 95% confidence interval, hence, considers normal distributions with a large sample size with estimates of:

- systematic uncertainty, also called bias (B_r) is calculated as Root Sum of Square (RSS) of each elementary error source (*i.e.*, calibration, data acquisition, data reduction, and conceptual bias) group of bias error. The elementary error sources have been divided and separately estimated;
- random uncertainty, also called precision uncertainty, (P_r), has been calculated for each run, according to $P_j(S) = KSDev_j$ where $SDev_j$ represents the standard deviation of j^{th} run, and $K=2$ according to the above-mentioned methodology;
- total uncertainty U_r is a RSS of B_r and P_r.

The bias, precision, and the uncertainties for nondimensional coefficients (R_{TM}/Δ, τ, $Z/V^{1/3}$, $S_W/\nabla^{2/3}$ and Fr_∇) are summarized in Table A5 below reported.

Appendix C. Numerical uncertainty analysis

The validation uncertainty (U_V) is given by

$$U_V^2 = U_D^2 + U_{SN}^2, \tag{3}$$

where U_D is the uncertainty of the experimental data.

The comparison error (E) is defined as the difference between the experimental data (D) and numerical simulation result (S_n), as reported below:

$$E = D - S_n. \tag{4}$$

According to ITTC procedures [36], numerical simulation uncertainty U_{SN} is mainly composed of iterative (U_I), grid (U_G), and time-step (U_{TS}) uncertainty, as follows:

$$U_{SN}^2 = U_I^2 + U_G^2 + U_{TS}^2. \tag{5}$$

According to Wilson et al. [37], the most important source of uncertainty of the numerical results is the grid.

The sources of uncertainty were evaluated for each of the simulation technique, *i.e.*, overset grid and morphing grid.

The numerical uncertainty evaluation was performed by using two different methods: the Grid Convergence Index (GCI) method and the Correction Factor (CF) method.

The general form of the uncertainty evaluation, based on the generalized Richardson Extrapolation (RE) method, can be written as follows:

$$U_k = F_S \left| \frac{\varepsilon_{21_k}}{r_k^{p_k} - 1} \right|, \tag{6}$$

where ε_{21k} is the solution changes for the k-input parameter between the solutions fine (S_{n1k}) to medium (S_{n2k}) and coarse (S_{n3k}), r_k is the constant refinement ratio, p_k is the observed order of accuracy, and F_S is the safety factor.

Furthermore, another parameter is the convergence ratio (R_k), which provides information about the convergence/divergence of a solution. The R_k value was determined by the following ratio:

$$R_k = \varepsilon_{21_k} / \varepsilon_{32_k}. \tag{7}$$

There are four kinds of possible convergence conditions: monotonic convergence ($0 < R_k < 1$), oscillatory convergence ($R_k < 0$ and $|R_k| < 1$), monotonic divergence ($R_k > 1$), and oscillatory divergence ($R_k < 0$ and $|R_k| > 1$). Since $0 < R_k < 1$, the monotonic convergence is satisfied.

The two different solution verification methods used in this study differ in the choice of the safety factor (F_S).

The GCI method in Eq. (7), proposed by [38,39], is used extensively and is recommended, for example, by the American Society of Mechanical Engineer (ASME) [40] and the American Institute of Aeronautics and Astronautics (AIAA) [41]. Roache recommended for three or more grids analyzed 1.25 as F_S value.

The other method used is the CF in Eq. (8), as discussed in [42], which uses a variable value of F_S, called correction factor (C_k). In the CF method, the uncertainty of the error depends on how much the solutions are close to the asymptotic range. The expressions defined the uncertainties were reported by [43]:

$$U_k = 1.25 \cdot \left| \frac{\varepsilon_{21_k}}{r_k^{p_k} - 1} \right|, \tag{8}$$

$$U_k = \begin{cases} \left[9.6(1 - C_k)^2 + 1.1\right] \left| \dfrac{\varepsilon_{21_k}}{r_k^{p_k} - 1} \right|, & |1 - C_k| < 0.125 \\ \left[2|1 - C_k| + 1\right] \left| \dfrac{\varepsilon_{21_k}}{r_k^{p_k} - 1} \right|, & |1 - C_k| \geq 0.125 \end{cases}. \tag{9}$$

Table A5
Experimental uncertainty analysis.

Description	Term	Speed								Units
		1.290	2.357	3.131	4.629	5.368	6.336	7.300	8.054	[m/s]
Model Speed										
	Fr_∇	1.077	1.968	2.614	3.864	4.481	5.289	6.094	6.723	[adim]
	B_V	6.97E-04	6.97E-04	3.13E-03	4.62E-03	5.36E-03	6.33E-03	7.29E-03	8.05E-03	[adim]
		22.62%	8.05%	4.73%	2.22%	1.66%	1.20%	0.90%	0.74%	% of $B_{Fr\nabla}$
	B_∇	1.29E-03	2.35E-03	3.13E-03	4.62E-03	5.36E-03	6.33E-03	7.29E-03	8.05E-03	[adim]
		77.38%	91.95%	95.27%	97.78%	98.34%	98.80%	99.10%	99.26%	% of $B_{Fr\nabla}$
	$B_{Fr\nabla}$	1.47E-03	2.46E-03	3.20E-03	4.68E-03	5.41E-03	6.37E-03	7.33E-03	8.08E-03	[adim]
		0.14%	0.12%	0.12%	0.12%	0.12%	0.12%	0.12%	0.12%	% of Fr_∇
	$P_{Fr\nabla}$	4.38E-03	4.80E-03	5.22E-03	1.08E-02	1.36E-02	1.41E-02	2.08E-02	2.50E-02	[adim]
	$U_{Fr\nabla}$	4.61E-03	5.39E-03	6.13E-03	1.18E-02	1.47E-02	1.54E-02	2.21E-02	2.63E-02	[adim]
		0.43%	0.27%	0.23%	0.30%	0.33%	0.29%	0.36%	0.39%	% of Fr_∇
Model Resistance Ratio										
	R_{TM}/Δ	0.100	0.178	0.204	0.256	0.312	0.407	0.491	0.555	[N/N]
	B_R	6.62E-04	6.68E-04	6.71E-04	6.78E-04	6.86E-04	7.05E-04	7.25E-04	7.42E-04	[N/N]
		97.49%	97.54%	97.56%	97.61%	97.67%	97.78%	97.90%	98.00%	% of $B^2_{RT/\Delta}$
	B_Δ	1.06E-04	1.06E-04	1.06E-04	1.06E-04	1.06E-04	1.06E-04	1.06E-04	1.06E-04	[N/N]
		2.51%	2.46%	2.44%	2.39%	2.33%	2.22%	2.10%	2.00%	% of $B^2_{RT/\Delta}$
	P_R	4.08E-05	1.54E-07	1.54E-07	3.45E-07	2.25E-06	2.25E-06	2.25E-06	1.53E-06	[N/N]
	$U_{RTM/\Delta}$	6.72E-04	6.76E-04	6.79E-04	6.86E-04	6.95E-04	7.13E-04	7.33E-04	7.50E-04	[N/N]
		0.67%	0.38%	0.33%	0.27%	0.22%	0.18%	0.15%	0.14%	% of R_T/Δ
Trim Angle										
	τ	2.23	3.55	3.27	3.27	2.87	2.69	2.52	2.58	[deg]
	$B_{\tau\text{-}cw}$	0.001	0.001	0.001	0.001	0.001	0.001	0.001	0.001	[deg]
		0.01%	0.01%	0.01%	0.01%	0.01%	0.01%	0.01%	0.01%	% of $B_\tau{}^2$
	$B_{\tau-ix}$	0.050	0.050	0.050	0.050	0.050	0.050	0.050	0.050	[deg]
		33.33%	33.33%	33.33%	33.33%	33.33%	33.33%	33.33%	33.33%	% of $B_\tau{}^2$
	$B_{\tau-iy}$	0.050	0.050	0.050	0.050	0.050	0.050	0.050	0.050	[deg]
		33.33%	33.33%	33.33%	33.33%	33.33%	33.33%	33.33%	33.33%	% of $B_\tau{}^2$
	$B_{\tau-iz}$	0.050	0.050	0.050	0.050	0.050	0.050	0.050	0.050	[deg]
		33.33%	33.33%	33.33%	33.33%	33.33%	33.33%	33.33%	33.33%	% of $B_\tau{}^2$
	B_τ	0.087	0.087	0.087	0.087	0.087	0.087	0.087	0.087	[deg]
		3.88%	2.44%	2.65%	2.65%	3.02%	3.22%	3.44%	3.36%	% of $B_\tau{}^2$
	P_τ	0.004	0.003	0.003	0.004	0.012	0.014	0.012	0.012	[deg]
	U_τ	0.087	0.087	0.087	0.087	0.087	0.088	0.087	0.087	[deg]
		3.89%	2.44%	2.65%	2.65%	3.04%	3.26%	3.47%	3.39%	% of τ
Sinkage										
	$Z/\nabla^{1/3}$	−0.080	0.010	0.048	0.085	0.139	0.147	0.151	0.181	[mm/mm]
	$B_{ZCG\text{-}cw}$	0.1	0.1	0.1	0.1	0.1	0.1	0.1	0.1	[mm]
		3.3E-03	3.3E-03	3.3E-03	3.3E-03	3.3E-03	3.3E-03	3.3E-03	3.3E-03	% of $B_{ZCG}{}^2$
	$B_{ZCG\text{-}lf}$	1.00	1.00	1.00	1.00	1.00	1.00	1.00	1.00	[mm]
		0.33	0.33	0.33	0.33	0.33	0.33	0.33	0.33	% of $B_{ZCG}{}^2$
	$B_{ZCG\text{-}la}$	1.00	1.00	1.00	1.00	1.00	1.00	1.00	1.00	[mm]
		0.33	0.33	0.33	0.33	0.33	0.33	0.33	0.33	% of $B_{ZCG}{}^2$
	$B_{ZCG\text{-}lb}$	1.00	1.00	1.00	1.00	1.00	1.00	1.00	1.00	[mm]
		0.332	0.332	0.332	0.332	0.332	0.332	0.332	0.332	% of $B_{ZCG}{}^2$
	B_{ZCG}	1.735	1.735	1.735	1.735	1.735	1.735	1.735	1.735	[mm]
		14.85%	114.14%	24.96%	14.03%	8.51%	8.07%	7.83%	6.56%	% of $B_{ZCG}{}^2$
	P_{ZCG}	6.365	7.120	6.846	4.046	8.755	5.870	6.556	4.864	[mm]
	$B_{Z/\nabla}{}^{1/3}$	0.016	0.012	0.014	0.017	0.023	0.024	0.025	0.028	[mm/mm]
		20.64%	115.04%	28.79%	20.06%	16.67%	16.45%	16.34%	15.77%	% of $Z/\nabla^{1/3}$
	$P_{Z/\nabla}{}^{1/3}$	0.025	0.024	0.024	0.019	0.036	0.030	0.032	0.032	[mm/mm]
	$U_{Z/\nabla}{}^{1/3}$	0.030	0.027	0.028	0.025	0.043	0.038	0.040	0.043	[mm/mm]
		−37.26%	261.37%	58.95%	29.82%	30.96%	26.01%	26.56%	23.52%	% of $Z/\nabla^{1/3}$
Model geometry										
	$S/\nabla^{2/3}$	6.730								
	B_S	0.284								[m^2/m^2]
		80.81%								% of $B^2_{S/\nabla 2/3}$
	$B_\nabla{}^{2/3}$	0.138								[m^2/m^2]
		19.19%								% of $B^2_{S/\nabla 2/3}$
	$P_{S/\nabla}{}^{2/3}$	0.032								[m/m]
	$U_{S/\nabla}{}^{2/3}$	0.317								[m^2/m^2]
		4.72%								%of $S/\nabla^{2/3}$
Density										
	ρ	1000								[kg/m^3]
	B_{r1}	0.071								[kg/m^3]
		1.15%								% of $B_\rho{}^2$
	B_{r2}	0.07								[kg/m^3]
		1.12%								% of $B_\rho{}^2$
	B_{r3}	0.655								[kg/m^3]

Table A5 (*Continued*)

Description	Term	Speed								Units
		1.290	2.357	3.131	4.629	5.368	6.336	7.300	8.054	[m/s]
		97.74%								% of B_p^2
	B_r	0.663								[kg/m^3]
		0.066%								% of B_r
	P_r	1.00								[kg/m^3]
	U_ρ	1.20								[kg/m^3]
		0.12%								% of r

Table A6
Overset grid case: uncertainty analysis.

	Grid ratio	R_G	p_G	$\%U_G$ GCI	$\%U_G$ CF	$\%U_{SN}$	$\%U_D$	$\%U_V$	$\%\|E\|$
R_{TM}/Δ	$\sqrt{2}$	0.47	1.44	9.06	16.62	16.62	0.27	16.6	3.8
τ	$\sqrt{2}$	0.43	−2.45	3.23	0.37	3.23	2.65	4.2	3.7
$Z/\nabla^{1/3}$	$\sqrt{2}$	1.65	−2.16	N.A.	N.A.	N.A.	29.82	N.A.	42.1
$S/\nabla^{2/3}$	$\sqrt{2}$	0.89	−0.34	0.96	0.60	0.96	4.72	4.8	31.0

U_G was expressed as a percentage value of the simulation solution for the finest grid.

Table A7
Morphing grid case: uncertainty analysis.

	Grid ratio	R_G	p_G	$\%U_G$ GCI	$\%U_G$ CF	$\%U_{SN}$	$\%U_D$	$\%U_V$	$\%\|E\|$
R_{TM}/Δ	$\sqrt{2}$	0.46	−2.27	6.92	0.49	6.92	0.27	6.9	18.3
τ	$\sqrt{2}$	0.78	−0.71	25.69	11.59	25.69	2.65	25.8	9.9
$Z/\nabla^{1/3}$	$\sqrt{2}$	0.90	−0.30	43.77	28.14	43.77	29.82	52.9	43.1
$S/\nabla^{2/3}$	$\sqrt{2}$	0.95	−0.14	13.65	11.95	13.65	4.72	14.4	53.2

U_G was expressed as a percentage value of the simulation solution for the finest grid.

References

[1] D. Savitsky, M. Morabito, Surface wave contours associated with the forebody wake of stepped planing hulls, Mar. Technol. 47 (January) (2010) 1–16.
[2] O.M. Faltinsen, Hydrodynamics of High-Speed Marine Vehicles, Cambridge Univeristy Press, New York, 2006.
[3] A. Sverchkov, Application of air cavities on high-speed ships in Russia, in: International Conference on Ship Drag Reduction (SMOOTH-Ships), Istanbul, 2010.
[4] D. Tauton, D. Hudson, R. Shenoi, Characteristics of series of high speed hard chine planing hulls-part 1: performanc in calm water, Int. Small Craft Technol. 152 (2010) 55–75.
[5] D. Svahn, Performance Prediction of Hulls with Transverse Steps (M.Sc. Thesis), KTH Centre for Naval Architecture, Stockolm, Sweden, 2009.
[6] W.R. Garland, K.J. Maki, A numerical study of a two-dimensional stepped planing surface, Jo. Ship Prod. 28 (2) (2012) 60–72.
[7] M.V. Makasyeyev, Numerical modeling of cavity flow on bottom of a stepped planing hull, in: Proceedings of the 7th International Symposium on Cavitation (CAV 2009), Ann Arbour, 2009.
[8] K.I. Matveev, Two-dimensional modeling of stepped planing hulls with open and pressurized air cavities, Int. J. Naval Archit. Ocean Eng. 4 (2) (2012) 162–171.
[9] K.I. Matveev, Hydrodynamic modeling of semi-planing hulls with air cavities, Int. J. Naval Archit. Ocean Eng. 3 (3) (2015) 500–508.
[10] S. Brizzolara, A. Federici, Designing of planing hulls with longitudinal steps: CFD in support of traditional semi-empirical methods, in: Proceedings of Design and Construction of Super & Mega Yachts, Genoa, 2013.
[11] P. Lotfi, M. Ashrafizaadeh, R.K. Esfahan, Numerical investigation of a stepped planing hull in calm water, Ocean Eng. 94 (2015) 103–110.
[12] M. Bakhtiari, S. Veysi, H. Ghassemi, Numerical modeling of the stepped planing hull in calm water, Int. J. Eng. Trans. B 29 (2) (2016).
[13] F. Stern, J. Yang, Z. Wang, H. Sadat-Hosseini, M. Mousaviraad, S. Bhushan, T. Xing, Computational ship hydrodynamics: nowadays and way forward, in: Symposium on Naval Hydrodynamics, Gothenburg, 2012.
[14] CD-adapco, STAR CCM+ User's Guide Version 9.06, 2014.
[15] S. Brizzolara, D. Villa, CFD simulation of planing hulls, in: 7th International Conference On High-Performance Marine Vehicles, Melbourne October 11–15, 2010.
[16] F. De Luca, S. Mancini, S. Miranda, C. Pensa, An extended verification and validation study of CFD simulations for planing hulls, J. Ship Res. 60 (2) (2016) 101–118.
[17] J.Y. Kang, B.S. Lee, Mesh-Based morphing method for rapid hull form generation, Comput.-Aided Des. 42 (2010) 970–976.
[18] M.E. Biancolini, I.M. Viola, Sails trim optimisation using CFD and RBF mesh morphing, Computers & Fluids 93 (2014) 46–60.
[19] ITTC, Recommended Procedures and Guidelines 7.5-01-01-01, 2002.
[20] L. Vitiello, S. Miranda, Towing Tank Test of Stepped Hull C03, University of Naples Federico II, Italy, 2017 [Online] Available: https://doi.org/10.6084/m9.figshare.4707697.v2 (Accessed 2017).
[21] ITTC, Recommended Procedures and Guidelines 7.5-02-02-01, 2011.
[22] L. Vitiello, S. Miranda, Propulsive performance analysis of a stepped hull by model test results and sea trial data, in: High Speed Marine Vehicles Symposium, Napoli, 2014, ISBN 9788890611216.
[23] ITTC, Recommended Procedures and Guidelines 7.5-02-02-02, 2002.
[24] C. Bohm, A Velocity Prediction Procedure for Sailing Yachts Based on Integrated Fully Coupled RANSE-Free-Surface Simulations, Delft University, Delft, 2014.
[25] J. Ferziger, M. Peric, Computational Method for Fluid Dynamics, Springer-Verlaag, Berlin, 2003.
[26] V. Andrillion, B. Alessandrini, A 2D+T VOF fully coupled formulation for calculation of breaking free surface flow, Proceedings of the 24th Symposium on Naval Hydrodynamics (2003).
[27] I.M. Viola, R.G.Y. Flay, R. Ponzini, CFD analysis of the hydrodynamic performance of two candidate america's cup AC33 hulls, Int. J. Small Craft Technol. 154 (B1–B12) (2012).
[28] T. Tezdogan, Y.K. Demirel, P. Kellet, M. Khorasanchi, A. Incecik, Full-Scale unsteady RANS-CFD simulations of ship behaviour and performance in head seas due to slow steaming, Ocean Eng. 97 (2015) 186–206.
[29] ITTC, Recommended Procedures and Guidelines Practical Guidelines for Ship CFD Applications 7.5-03-02-03, 2011.
[30] S. Mancini, The Problem of the Verification and Validation Processes of CFD Simulations of Planing Hulls – PhD Thesis, University of Naples, Federico II, Naples, 2016.
[31] C. Bertorello, E. Begovic, S. Mancini, Hydrodynamic performances of small size swath craft, Brodogr. Shipbuild. 66 (4) (2015).
[32] A. de Boer, M.S. Schoot, H. Bijl, Mesh morphing based on radial function interpolation, Comput. Struct. 85 (2007) 784–795.
[33] E.L. Amromin, Analysis of interaction between ship bottom air cavity and boundary layer, Appl. Ocean Res. 59 (2016) 451–458.
[34] S.M. Mousaviraad, Z. Wang, F. Stern, URANS studies of hydrodynamic performance and slamming loads on high-Speed planing hulls in calm water and waves for deep and shallow conditions, Appl. Ocean Res. 51 (2015) 222–240.
[35] H. Coleman, W. Steele, Experimental and Uncertainty Analysis for Engineers, 2nd ed., New York, NY, John Wiley & Sons, 1999.
[36] ITTC, Uncertainty Analysis in CFD Verfication an Validation 7.5-03-01-01, 2008.
[37] R.V. Wilson, F. Stern, H.W. Coleman, E.G. Paterson, Comprehensive approach to verification and validation of CFD simulations – part 2: application for RANS simulation of a Cargo/Container ship, J. Fluids Eng. 123 (2001) 803–810.

[38] P.J. Roache, Verification and Validation in Computational Science and Engineering, Hermosa Publishers, New Mexico, 1998.
[39] P.J. Roache, Code verification by the method of manufactured solutions, J. Fluids Eng. 1 (124) (2002) 4–10.
[40] I.B. Celik, U. Ghia, P.J. Roache, C.J. Freitas, H. Coleman, P.E. Raad, Procedure for estimation and reporting of uncertainty due to discretization in CFD applications, J. Fluids Eng.-Trans. ASME 130 (2008).
[41] R.R. Cosner, W.L. Oberkampf, C.L. Rumsey, C. Rahaim, T. Shih, AIAA Committee on Standards for Computational Fluid Dynamics: Status and Plans, 2006, Reno, NV, USA.
[42] F. Stern, R.V. Wilson, H.W. Coleman, E.G. Paterson, Comprehensive approach to verification and validation of CFD simulations – part 1: methodology and procedures, J. Fluids Eng. 123 (December) (2001) 793–802.
[43] R. Wilson, J. Shao, F. Stern, Discussion: criticism of the correction factor, J. Fluids Eng. 126 (2004).